Expert Systems With Applications 333 (2027) 133814

Contents lists available at ScienceDirect

Expert Systems With Applications

journal homepage: www.elsevier.com/locate/eswa

# Optimizing cruising speed for energy-efficient and safe operation of metro-based underground logistics systems using a surrogate-assisted multi-objective evolutionary algorithm

Duo Zhang [b], Gisella Tomasini [b], Yuan-Peng He [c], Fang-Ru Zhou [b,d], Zi-Yu Tao [a,*]

[a] School of Mechanical and Electrical Engineering, Guangzhou University, Guangzhou, the People's Republic of China
[b] Department of Mechanical Engineering, Politecnico di Milano, Milan, Italy
[c] School of Mechanical Engineering, Southwest Jiaotong University, Chengdu, the People's Republic of China
[d] School of Transportation & Logistics, Southwest Jiaotong University, Chengdu, the People's Republic of China

ARTICLE INFO

*Keywords:*
Underground logistics system
Operation safety
Energy efficiency
Multibody dynamics
Random Forest
Bi-objective optimization

ABSTRACT

The metro-based underground logistics system (ULS) offers an effective solution to alleviate traffic congestion, environmental degradation, and energy inefficiency caused by intensive road-based freight transport. Unlike passengers, cargo exhibits variable mass properties, significantly influencing the dynamic performance of metro vehicles. To enhance both operation safety and energy efficiency of metro-based ULS, this study proposes an AI-driven optimization framework for optimizing the cruising speed of metro vehicles using multibody dynamics (MBD), Random Forest (RF) surrogate modeling, and adaptive reference point-based multi-objective evolutionary algorithm (AR-MOEA) that establishes a complete intelligent decision pipeline. MBD simulations under 5625 designed working conditions generate training data covering comprehensive working conditions. An RF-based surrogate model learns the complex vehicle dynamics to enable rapid performance prediction. AR-MOEA optimizes cruising speeds across segments in 4.9 s to simultaneously improve safety and energy efficiency. Compared to a uniform speed profile, the proposed AI-powered strategy can improve the operation safety by up to 23.51 % and energy efficiency by up to 20.75 %. This study provides valuable insights for the sustainable development of metro-based ULS.

## 1. Introduction

### 1.1. Background and motivation

Urban logistics has become a critical bottleneck for sustainable urban development, characterized by a triad of interconnected challenges: traffic congestion, environmental degradation, and energy inefficiency. Specifically, road-based freight transport accounts for approximately 30 %-40 % of traffic congestion and 25 % of mobility-related greenhouse gas (GHG) emissions (Muñoz-Villamizar et al., 2020; Coulombel et al., 2018). In recent years, these adverse effects have intensified due to rapid urbanization and e-commerce growth. Therefore, exploring innovative, sustainable, and efficient alternatives for freight distribution is imperative (Di et al., 2022).

In response to these challenges, attention has turned to underground space as a potential solution, leading to the concept of the underground logistics system (ULS) (Hu et al., 2025; Li & Yuen, 2025). Typically, ULS is an independent system comprising dedicated tunnels or pipelines and specially designed transport units (Visser, 2018). However, implementing the ULS is not straightforward. The primary challenge involves multi-faceted coordination across urban planning, logistics management, and public infrastructure. This complexity results in high initial costs, intricate engineering, and prolonged construction periods (Di et al., 2022). In contrast, metro systems, known for their efficiency and environmental benefits, often have surplus capacity during off-peak hours. Utilizing this capacity for urban freight transport presents an opportunity to optimize resources without additional infrastructure investment (Hu et al., 2023). Thus, the metro-based ULS, illustrated in Fig. 1, has emerged as a viable and effective approach to mitigating urban logistics issues.

* Corresponding author.
*E-mail addresses:* duo.zhang@polimi.it (D. Zhang), gisella.tomasini@polimi.it (G. Tomasini), he.yuanpeng@swjtu.edu.cn (Y.-P. He), fangru.zhou@mail.polimi.it (F.-R. Zhou), ziyu.tao@gzhu.edu.cn (Z.-Y. Tao).

https://doi.org/10.1016/j.eswa.2026.133814
Received 4 April 2026; Received in revised form 30 June 2026; Accepted 28 July 2026
Available online 30 July 2026

**Fig. 1.** The example of metro-based ULS (Xinhua News Agency, 2025).

Unlike passengers, cargo characteristics, e.g. size, density, and center of gravity, are highly variable. In particular, cargo distribution changes with loading and unloading at each station, whereas passengers tend to distribute themselves more uniformly within the vehicle to maximize personal space and minimize physical contact with others. Since vehicle-cargo interaction significantly affects wheel-rail contact forces, the influence of load characteristics on metro vehicle performance warrants detailed investigation. Consequently, the operation of metro-based ULS should incorporate these effects to enhance both operation safety and energy efficiency. Given the underground setting and low operating speed of ULS, the influence of wind forces is considered negligible in this research.

### 1.2. Literature review

To the best of our knowledge, existing research on metro-based ULS operations has primarily focused on tactical and strategic aspects, such as network planning and urban co-modality. For instance, An et al. (2024) developed a Wasserstein distributionally robust optimization model to schedule freight trains and assign cargo within a metro-based ULS, effectively managing demand uncertainty while minimizing operating costs through strategies like flexible skip-stopping. Chen et al. (2023) developed a decision-making framework integrating benefit quantification, stakeholder dynamics, and network optimization to plan the metro-based ULS. Di et al. (2022) presented an optimization framework to simultaneously determine carriage allocation and passenger-freight flow control for minimizing operational costs and delays during off-peak hours. Behiri et al. (2018) proposed an optimization and simulation framework to assess the feasibility of integrating urban freight transportation into existing passenger rail systems, focusing on scheduling, resource utilization, and operational impacts. However, few studies have addressed the operational control of metro vehicles used for freight transport, especially considering the impact of carriage.

To elucidate the relationship between loading offset and operation safety, a quasi-static analysis of a loaded wagon negotiating a curve at constant speed was conducted, deriving an analytical expression between the three-dimensional center of gravity and the wheel unloading ratio (Zhang et al., 2021b). Building on this, a wagon-cargo coupling model was developed to incorporate changes in the moment arm and shifts in the center of rotation due to variations in the center of gravity (Zhang et al., 2019). Multibody dynamics (MBD) simulations confirmed that the loaded wagon's center of gravity must remain within a safety space, determined by cruising speed, to ensure operation safety (Zhang et al., 2022). Beyond loading offset, cargo density and quantity also influence wheel-rail interaction. For high-speed freight trains, increasing cargo density and quantity generally improves operation safety (Zhang, D. et al., 2023a; Zhang, D. et al., 2024c).

Actually, the coupling relationship between the cargo and vehicle not only affects the operation safety significantly, but also plays an important role in the energy efficiency of trains. (Zhang et al., 2023b) proposed a model to evaluate the energy consumed by motion resistances (ECMR) using MBD simulations. Subsequent work demonstrated the effect of loading offset on ECMR under varying speeds and curve radii (Zhang et al., 2023c).

Although prior studies have proved that running performance of trains is affected by load characteristics (i.e., loading offset, density, and quantity) and running conditions (i.e., speed and curve radius), a practical and efficient method for improving loaded vehicle performance remains lacking. Among these factors, vehicle speed is the most readily controllable (Zhou et al., 2024; Zou et al., 2025). Kinds of train operation control strategies have been proposed to save the energy consumption of trains. Feng et al. (2022) proposed a convex optimization formulation for the energy-efficient train control problem, addressing the computational bottleneck that limits online applications of existing methods. Xiao et al. (2023) proposed a computationally efficient approach to minimize total electrical energy consumption from traction substations. A real-time iteration sequential quadratic programming algorithm was proposed, yielding near-optimal solutions with high computational efficiency. Chen et al. (2023) addressed the challenge of simultaneously achieving timetable adherence and energy efficiency in high-density metro lines subject to frequent disturbances. A hierarchical optimal control framework was proposed based on the model predictive control method. Peng et al. (2024) proposed a realistic model incorporating hybrid braking characteristics and reduced-power characteristics at high speeds into the energy-efficient train control problem to improve both control precision and modeling accuracy of energy consumption and time. Although various models were established and different algorithms were proposed, the fundamental simplification of these energy consumption models is regarding the train as a single particle. Thus, the internal forces of the vehicle, e.g. spring and damping forces, are overlooked, and the wheel-rail forces are idealized. The effects of loading characteristics on the energy consumption of trains are neglected. Consequently, previous control algorithms are not applicable to the real-time, dynamic, and uncertain underground logistics scenarios.

Meanwhile, advanced weigh-in-motion (WIM) systems have matured, enabling accurate real-time measurement of wheel loads (D'Adamio et al., 2016). For example, Obrien et al. (2018)evaluated the accuracy of two independent WIM systems, while Allotta et al. (2015) developed a method for estimating axle and wheel loads at high vehicle speeds based on vertical forces on track sleepers, then deriving the center-of-gravity position of the railway vehicle. With WIM systems, load characteristics can be assessed conveniently and transmitted to the decision system wirelessly, making it feasible to optimize vehicle speed in real time according to the obtained load characteristics for enhanced running performance of metro-based ULS. In practice, WIM systems for moving rail vehicles are subject to sensor noise, latency, and calibration drift. Typical inaccuracies are within $\pm$ 5 % for axle load measurements (ISWIM, 2020). Advanced algorithms can achieve estimation errors below 2 % under favorable conditions (D'Adamio et al., 2016). Even though the error is acceptable, WIM systems should be periodically calibrated using static weighing references to maintain accuracy. Multiple measurement stations can be placed along the track to improve reliability through redundancy.

In metro-based ULS, speed optimization must be performed online based on real-time measurements from WIM systems rather than offline based on fixed schedules. This real-time requirement rules out traditional offline approaches that pre-compute a single speed profile for the entire journey. Instead, the optimization framework must be capable of predicting vehicle performance for any loading condition instantaneously. This is a task that MBD simulation cannot fulfill within the required time window. Recent advances in machine learning-based predictive modeling have demonstrated the power of data-driven approaches for complex engineering systems. Wu, J. et al. (2025) proposed a multi-view fully connected graph approach to fuse multi-sensor signals for remaining useful life prediction of mechanical equipment, showcasing how advanced neural network architectures can model system degradation patterns from heterogeneous sensor data. Furthermore, digital twin frameworks have been increasingly applied to railway systems for performance prediction, predictive maintenance and fault diagnosis (Guo et al., 2026; He et al., 2025a,b), establishing the viability of virtual-physical mapping for real-time decision support. In the domain of train operation optimization, deep reinforcement learning and bi-objective optimization methods have been applied to metro train control for energy conservation and timetable rescheduling under uncertainty (Sun et al., 2024; Tan et al., 2025). These studies collectively demonstrate the growing integration of AI and optimization techniques in railway engineering, yet none address the specific challenge of dynamically optimizing cruising speed in response to real-time, structurally uncertain cargo loading conditions.

### 1.3. Contributions

To improve the operation safety and energy efficiency of metro-based ULS, this study proposes an AI-driven optimization framework that integrates MBD simulation, Random Forest (RF) surrogate modeling, and adaptive reference point-based multi-objective evolutionary algorithm (AR-MOEA) into a closed-loop intelligent decision pipeline. The main contributions are as follows:

(1) A novel MBD model for evaluating the running performance of loaded metro vehicles under comprehensive loading and running conditions.

Metro-based ULS represents a unique transport mode combining vehicle features of traditional metro trains and the load characteristics of freight wagons. For a typical metro vehicle, we built a special-designed MBD vehicle-cargo coupling model to evaluate its running performance under diverse loading and running conditions, including cargo quantity, lateral and longitudinal loading offsets, curve radius, and running speed. This is the first time the joint effects of loading offset and cargo quantity on railway vehicle running performance have been evaluated. Moreover, the variable cargo quantity introduces a significant challenge in designing the loading conditions for MBD simulations. The feasible longitudinal offset range changes with cargo height due to regulatory constraints, requiring a non-uniform experimental design across the loading parameter space. This represents a methodological breakthrough in railway freight transport simulation and provides a physics-based training data foundation for the AI-driven optimization pipeline.

(2) AI-based surrogate modeling for real-time performance prediction.

Using MBD simulation results under designed working conditions, surrogate models based on the Random Forest (RF) algorithm are developed to predict the operation safety and energy efficiency of metro vehicles under arbitrary conditions. The RF surrogate model serves as an AI-based digital twin of the MBD vehicle model. It learns the complex, nonlinear mapping from five input features to two performance indicators, enabling instantaneous performance prediction without rerunning computationally expensive MBD simulations. This capability is the essential enabler of the entire optimization pipeline, transforming the problem from one requiring hours of computation to one that can be solved in seconds. The accurate surrogate model is the foundation of real-time, online optimization for vehicle cruising speed, a capability that has not been previously demonstrated in surrogate-assisted railway optimization studies.

(3) A novel integration architecture for online, closed-loop speed optimization.

A bi-objective optimization model is formulated to determine the optimal cruising speed in real time given specific load characteristics and curve radii. Optimization objectives, maximizing operation safety and energy efficiency, are evaluated via the surrogate models. Using an adaptive reference point-based multi-objective evolutionary algorithm (AR-MOEA), optimal speeds are derived to simultaneously enhance operation safety and energy efficiency of metro-based ULS. Unlike existing studies that address offline, static design optimization, our framework tackles online, operational control that optimizes cruising speed dynamically in response to real-time WIM measurements of cargo mass, longitudinal offset, and lateral offset. This WIM-driven closed-loop capability enables the system to adapt to the inherent uncertainty and variability of freight operations, where loading conditions change stochastically at each station. Compared to uniform speed profiles, the proposed AI-powered strategy improves operation safety by up to 23.51 % and energy efficiency by up to 20.75 %.

The paper is structured as follows: **Section 2** outlines the research methodology. **Section 3** presents numerical simulation and analysis. **Section 4** details the surrogate model for performance prediction. **Section 5** formulates and solves the bi-objective optimization model for speed optimization.

## 2. Methodology

This study aims to develop a framework for sustainably optimizing train cruising speed in metro-based ULS according to load characteristics obtained from advanced data sources (e.g., WIM systems), as illustrated in Fig. 2. Based on MBD simulations under various conditions, the surrogate model is constructed using RF to dynamically predict vehicle performance. Upon receiving load characteristics from the WIM system, the surrogate model feeds predictions into an optimization model. Using AR-MOEA, the optimal cruising speed corresponding to specific load characteristics is determined. The proposed framework consists of three AI-enabled stages: (1) data generation via MBD simulation; (2) surrogate modeling using Random Forest to learn the vehicle's dynamic response; and (3) intelligent optimization using AR-MOEA to derive optimal speed profiles. This three-stage pipeline transforms the conventional offline, physics-based approach into an online, AI-driven decision system.

As noted in the **Introduction**, WIM systems are well-established in railways. Assuming accurate detection of load characteristics, this study focuses on the remaining three tasks of the proposed framework.

### 2.1. Dynamics equation of the loaded vehicle

This study considers a B-type metro vehicle, commonly used in metro systems. As illustrated in Fig. 3, the vehicle consists of one loaded carbody, two sideframes, and four wheelsets. There are primary and secondary suspensions systems between the wheelset and sideframe, sidefame and carbody respectively. The cargo shifts the carbody's center of gravity from point O (empty) to point C (loaded). The definitions of the symbols in Fig. 3 are listed in Table 1.

For a given metro vehicle, the position of C is depending on the load characteristics, as illustrated in Fig. 4, where O, $O^{\#}$, and C denote the gravity centers of the empty carbody, cargo, and loaded carbody respectively, $M_v$ and $M$ denote the masses of the empty carbody and cargo respectively, $M_c$ denotes the mass of loaded carbody and equals the sum of $M$ and $M_v$, $h$ denotes the height of the cargo model, $H_{floor}$ denotes the vertical distance from the vehicle floor to O, $x$ and $y$ denote the longitudinal and lateral loading offsets respectively, $x_c$ and $y_c$ denote the longitudinal and lateral distances from O to C respectively. The metro-based ULS is mainly used to transport the small cargoes, especially packages. Usually the cargoes with similar characteristics are typically located within the same area. But cargoes in different areas of the vehicle may have significant differences. Thus, the cargo is modeled as a cuboid with uneven horizontal mass distribution and uniform vertical distribution. Because the packaged goods (e.g., parcels, boxes, containers) are stacked in fixed configurations, secured by packaging that limits internal relative motion, and subject to load restraint

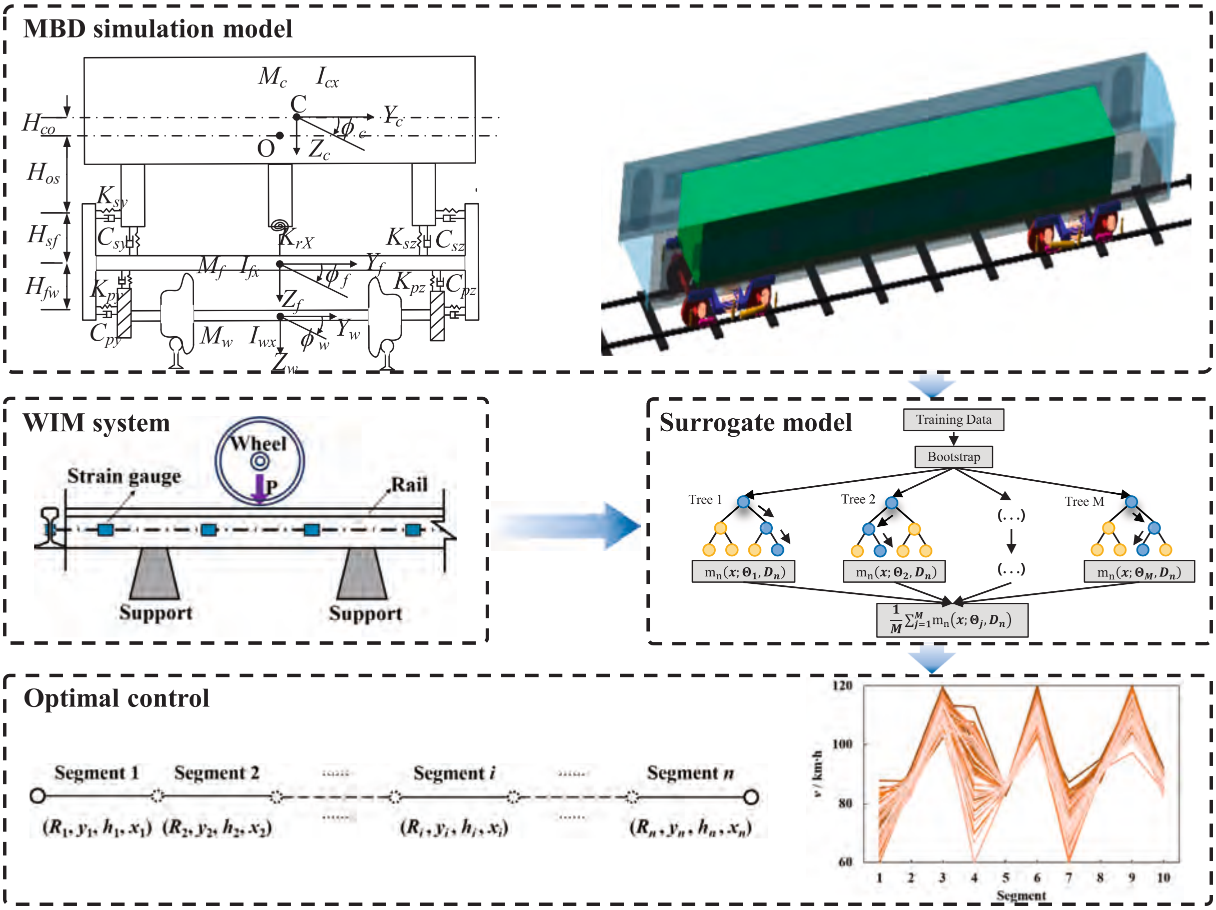


**Fig. 2.** Overview of the proposed framework.

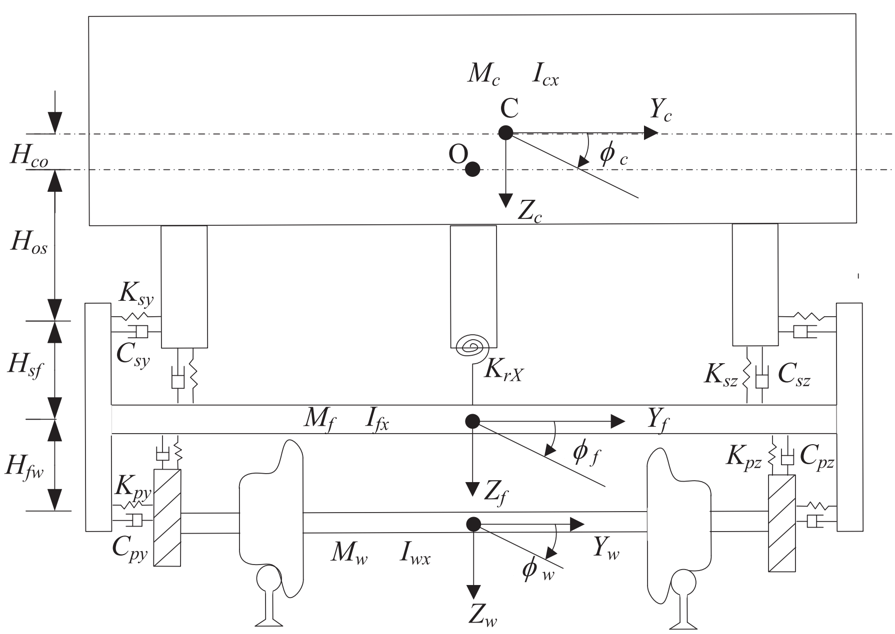

**Fig. 3.** The model of the loaded vehicle.

practices (e.g., dunnage, bracing, void fillers) that prevent shifting during transit, the nonlinear sloshing effects (e.g., fluid-like or granular sloshing effects) caused by loose stacking in real-world logistics are not considered. The vertical distance from the vehicle floor to $O^{\#}$ is $h/2$.

According to the formula for the gravity center, the position of C in three directions can be derived based on the load characteristics as:

Vertically,

**Table 1**
Definitions of symbols for the vehicle model.

| Symbol | Physical meaning |
|---|---|
| $Y_c$, $Y_f$, $Y_w$ | Lateral displacements of carbody, sideframe, and wheelset |
| $Z_c$, $Z_f$, $Z_w$ | Vertical displacements of carbody, sideframe, and wheelset |
| $\phi_c$, $\phi_f$, $\phi_w$ | The roll angles of carbody, sideframe, and wheelset |
| $M_c$,$M_f$, $M_w$ | The masses of carbody, sideframe, and wheelset |
| $I_{cx}$, $I_{fx}$, $I_{wx}$ | Mass moment of inertia of carbody, sideframe, and wheelset about X-axis |
| $K_{py}$, $K_{sy}$ | Lateral stiffness coefficients of primary and secondary suspensions |
| $K_{pz}$, $K_{sz}$ | Vertical stiffness coefficients of primary and secondary suspensions |
| $C_{py}$, $C_{sy}$ | Lateral damping coefficients of primary and secondary suspensions |
| $C_{pz}$, $C_{sz}$ | Vertical damping coefficients of primary and secondary suspensions |
| $K_{rX}$ | Stiffness coefficient of anti-roll spring |
| $H_{co}$ | Vertical distance between the centers of empty carbody and loaded carbody |
| $H_{os}$ | Vertical distance between the center of empty carbody and the secondary suspension |
| $H_{sf}$ | Vertical distance between the secondary suspension and the center of sideframe |
| $H_{fw}$ | Vertical distance between the centers of sideframe and wheelset |

$$H_{co} = \frac{Mh - 2MH_{floor}}{2(M + M_v)} \tag{1}$$

Longitudinally,

$$x_c = \frac{Mx}{M + M_v} \tag{2}$$

Laterally,

$$y_c = \frac{My}{M + M_v} \tag{3}$$

Given the substantial influence of cargo on the carbody's center of gravity, the dynamics equations of loaded carbody are updated from prior studies where the geometric center of carbody was assumed to coincide with the center of gravity (Zhang et al., 2024a; Zhang et al., 2024b; Zhang et al., 2021a; Ahmad et al., 2025; Bustos et al., 2025; D. Zhang et al., 2021a,2024a,2024b; P. Zhang et al., 2026). Generally, the loaded carbody is subject to various external forces and moments, as illustrated in Fig. 5 and defined in Table 2.

As shown in Fig. 4, the position of loaded vehicle's gravity center, which is affected by the load characteristics, can be clarified by its relative displacement to the empty vehicle's gravity center as $\overrightarrow{OC} = (x_c, y_c, -H_{co})$. When the vehicle negotiates the right-hand curved track whose radius is $R$ with the cruising speed of $v$, the equivalent curve radius corresponding to the loaded carbody is ($R$-$y_c$). Applying the Newton's second law, the dynamics equations of the loaded carbody are formulated as below.

- Lateral motion:

$$\begin{aligned} & M_c\left[\ddot{Y}_c + \frac{v^2}{R - y_c} + (r_0 + H_{co} + H_{os} + H_{sf} + H_{fw})\ddot{\phi}_{\sec}\right] \\ & = F^L_{ys1} + F^L_{ys2} + F^R_{ys1} + F^R_{ys2} + M_c g\phi_{\sec} \end{aligned} \tag{4}$$

- Vertical motion:

$$M_c[\ddot{Z}_c - (a_0 - y_c)\ddot{\phi}_{\sec} - \frac{v^2}{R - y_c}\phi_{\sec}] = -F^L_{zs1} - F^L_{zs2} - F^R_{zs1} - F^R_{zs2} + M_c g \tag{5}$$

- Roll motion:

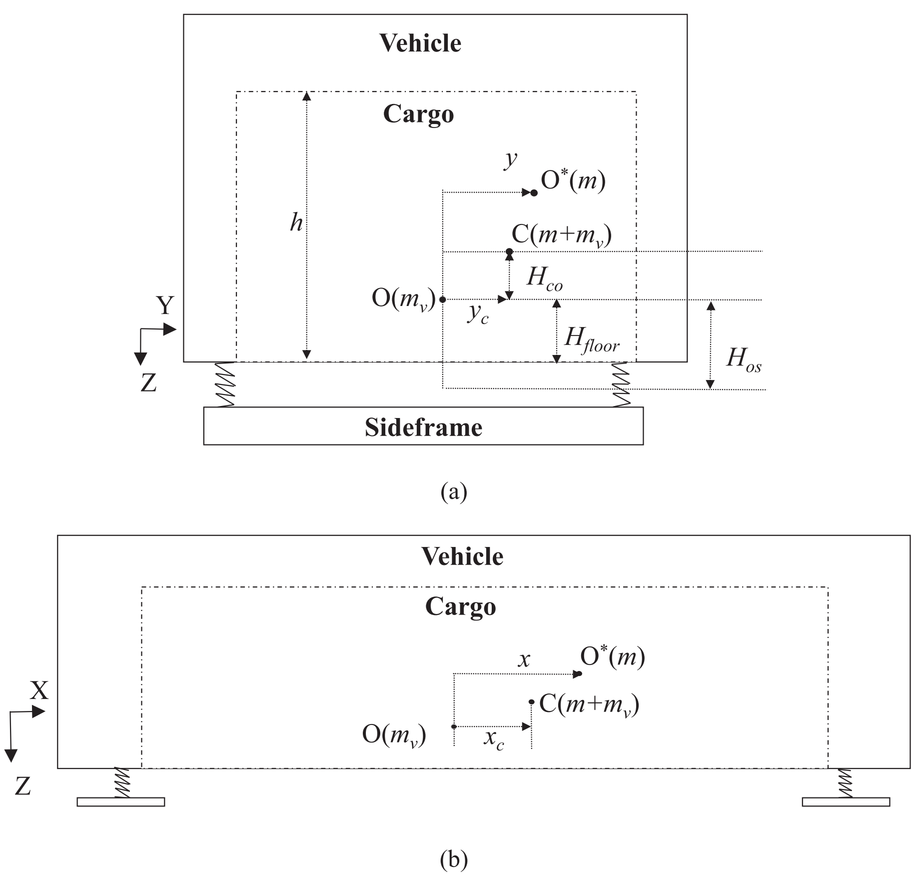


**Fig. 4.** Effects of loads on the gravity center of carbody: (a) front view, and (b) side view.

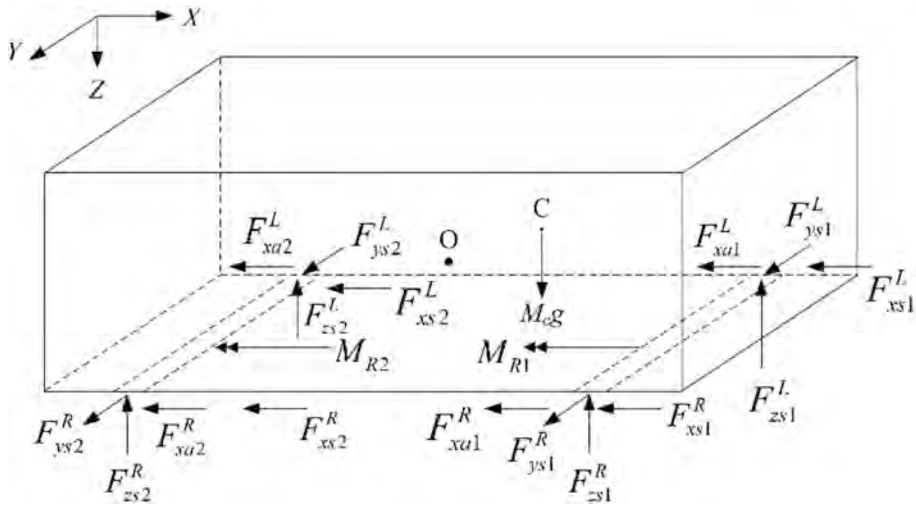


**Fig. 5.** Forces and moments applied to the carbody.

**Table 2**
Definitions of force symbols.

| Symbol | Physical meaning |
|---|---|
| $F^L_{xsi}$, $F^R_{xsi}$ | Left and right longitudinal forces at secondary suspension of the *i*th bogie |
| $F^L_{ysi}$, $F^R_{ysi}$ | Left and right lateral forces at secondary suspension of the *i*th bogie |
| $F^L_{zsi}$, $F^R_{zsi}$ | Left and right vertical forces at secondary suspension of the *i*th bogie |
| $F^L_{xai}$, $F^R_{xai}$ | Left and right longitudinal forces at anti-hunting dampers of the *i*th bogie |
| $M_{Ri}$ | Anti-roll torque of the *i*th bogie |

$$I_{cx}\left(\ddot{\phi}_c+\ddot{\phi}_{sec}\right) = -\left(F^L_{ys1}+F^L_{ys2}+F^R_{ys1}+F^R_{ys2}\right)(H_{co}+H_{os})+(F^L_{zs1}+F^L_{zs2})(d_s+y_c) - \left(F^R_{zs1}+F^R_{zs2}\right)(d_s-y_c)-M_{r1}-M_{r2} \tag{6}$$

- Pitch motion:

$$I_{cy}\ddot{\beta}_c = (F^L_{zs1}+F^R_{zs1})(l_b-x_c)-\left(F^L_{zs2}+F^R_{zs2}\right)(l_b+x_c)-\left(F^L_{xs1}+F^L_{xs2}+F^R_{xs1}+F^R_{xs2}\right)(H_{co}+H_{os})-\left(F^L_{xa1}+F^L_{xa2}+F^R_{xa1}+F^R_{xa2}\right)(H_{co}+H_{os}) \tag{7}$$

- Yaw motion:

$$I_{cz}[\ddot{\psi}_c+v\frac{d}{dt}(\frac{1}{R-y_c})] =(F^L_{ys1}+F^R_{ys1})(l_b-x_c)-(F^L_{ys2}+F^R_{ys2})(l_b+x_c)+\Big(F^R_{xs1}+F^R_{xs2})(d_s-y_c)+(F^R_{xa1}+F^R_{xa2})(d_{sc}-y_c)-(F^L_{xs1}+F^L_{xs2}\Big)(d_s+y_c)-(F^L_{xa1}+F^L_{xa2})(d_s+y_c) \tag{8}$$

Additional symbols in Eqs. (4)-(8) are introduced in Table 3.

The load characteristics do not have direct effect on the motions of sideframes and wheelsets. Hence, the dynamics equations of these components can be referenced from previous studies (Zhai et al., 2009; ZHAI, W., , 2019).

### 2.2. Multibody dynamics model of the metro vehicle

Using the commercial software VI-Grade, an MBD model of the metro vehicle is constructed based on the above equations, as shown in Fig. 6. The cargo is modeled as a cuboid with uneven horizontal mass distribution. The center of gravity and cargo height vary with loading conditions. A fixed joint connects the cargo to the carbody. Primary and secondary suspensions are modeled using appropriate forces, joints, and constraints. The S1002 wheel profile and UIC60 rail profile are adopted. Key vehicle parameters are listed in Table 4.

**Table 3**
Definitions of emerging symbols.

| Symbols | Physical meaning |
|---|---|
| $I_{cy}$ | Mass moment of inertia of carbody about Y-axis |
| $I_{cz}$ | Mass moment of inertia of carbody about Z-axis |
| $r_0$ | Nominal contact rolling radius of the wheel |
| $\phi_{sec}$ | The superelevation angle of the curve where the car body center locates |
| $g$ | Gravity acceleration |
| $l_b$ | Half-distance between bogie centers |
| $a_0$ | Half of track gauge |
| $\beta_c$ | The pitch angle of carbody |
| $\psi_c$ | The yaw angle of carbody |
| $d_s$ | Half-distance between the secondary suspension of the two sides of the bogie |
| $d_{sc}$ | Half-distance between the anti- hunting dampers on the two sides of the bogie |

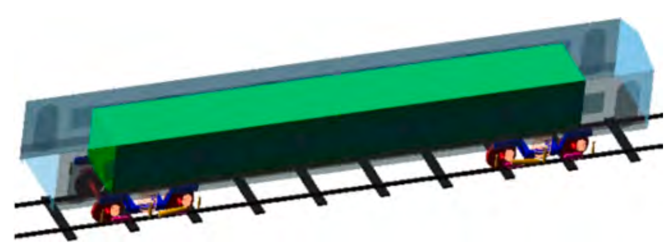

**Fig. 6.** The MBD model of the loaded vehicle.

To validate the model, an in-situ test was conducted for a B-type metro vehicle on Chengdu Metro Line 1 (Fig. 7). The empty vehicle traveled at 60 km/h on tangent track. Carbody accelerations were measured using three-axis piezoelectric accelerometers installed on the carbody floor. Data were acquired at a sampling frequency of 1000 Hz. Measurements were recorded continuously over a duration of 120 s during stable operation. Because the track condition of Chengdu Metro is similar as the German railway spectra of low irregularity (Chen & Wan, 2023), it is applied to the track model as the external excitations of the MBD vehicle model.

The comparison of the results between the MBD simulation and in-situ test are displayed in Fig. 8. The good agreement can indicate the accuracy of the MBD vehicle model.

**Table 4**
Values of key parameters for the vehicle model.

| Parameters | Value |
|---|---|
| Mass of empty carbody(kg) | 2.19E + 04 |
| Carbody rolling moment of inertia(kg · m$^2$) | 1.49E + 04 |
| Carbody pitching moment of inertia(kg · m$^2$) | 6.17E + 05 |
| Carbody yawing moment of inertia(kg · m$^2$) | 6.17E + 05 |
| Load limit stenciled on the car(kg) | 2.112E + 4 |
| Length of carbody (m) | 19 |
| Width of carbody (m) | 2.8 |
| Height of carbody (m) | 2.1 |
| Sideframe mass(kg) | 2550 |
| Sideframe rolling moment of inertia(kg · m$^2$) | 1050 |
| Sideframe pitching moment of inertia(kg · m$^2$) | 1750 |
| Sideframe yawing moment of inertia(kg · m$^2$) | 1980 |
| Wheelset rolling radius(m) | 0.42 |
| Wheel base (m) | 2.3 |
| Tape circle distance (m) | 1.493 |
| Axle length (m) | 2.6 |
| Distance between center pivots (m) | 12.6 |
| Wheelset mass(kg) | 1420 |
| Wheelset rolling moment of inertia(kg · m$^2$) | 985 |
| Wheelset pitching moment of inertia(kg · m$^2$) | 97 |
| Wheelset yawing moment of inertia(kg · m$^2$) | 985 |
| Primary spring longitudinal stiffness(MN/m) | 6.6 |
| Primary spring lateral stiffness(MN/m) | 10.4 |
| Primary spring vertical stiffness(MN/m) | 1.7 |
| Primary spring vertical damping(Ns/m) | 5000 |
| Secondary spring longitudinal stiffness(MN/m) | 0.13 |
| Secondary spring lateral stiffness(MN/m) | 0.13 |
| Secondary spring vertical stiffness(MN/m) | 0.28 |
| Secondary spring lateral damping(Ns/m) | 30,000 |
| Secondary spring vertical damping(Ns/m) | 40,000 |

**Fig. 7.** In-situ tests for the carbody vibration.

## 3. Numerical results and analysis

### 3.1. Design of working conditions

By means of the established MBD vehicle model, the running performance of metro vehicles can be evaluated. In order to imitate the complex realistic scenarios by MBD simulations, it is necessary to design comprehensive working conditions, including the running conditions and loading conditions.

#### 3.1.1. Running conditions configuration

In this study, the curve negotiation process on various tracks with different radii under different cruising speeds will be simulated to establish the predict model for the running performance of the metro vehicle in Section 4. Because the design speed of the adopted metro vehicle is 120 km/h and it is not necessary to restrict the cruising speed for the metro-based ULS to consider the requirement on passenger riding comfort, the maximum speed is set as 120 km/h. Moreover, the minimum speed of the metro vehicle running on the main line is 40 km/h (Ministry of Housing and Urban Rural Development of the People's Republic of China, 2013). Therefore, the ranges of the cruising speed are designed as 40, 60, 80 100, and 120 km/h.

The superelevation for all the curved tracks is set as 120 mm for negotiating curves with a high speed and simultaneously meeting with the safety requirements (Ministry of Housing and Urban Rural Development of the People's Republic of China, 2013). Because the maximum cruising speed is set as 120 km/h, the curve radius should not be smaller than 600 m to guarantee the operation safety (Ministry of Housing and Urban Rural Development of the People's Republic of China, 2013). Thus, the running performance of metro vehicles on five right-hand curved tracks will be tested, whose radii are 600, 900, 1200, 1500, and 1800 m respectively. The length of the transition curve is designed as 100 m according to the requirement for the 600-meter curved track. The length for all the curved tracks is 360 m. The German railway spectra of low irregularity introduced in Section 2.2 are adopted as the external excitation in the simulations.

In conclusion, the radius of curved tracks (denoted by $R$) and cruising speed of the metro vehicle (denoted by $v$) are two parameters which can represent the running conditions. Their ranges are listed in Table 5.

#### 3.1.2. Loading conditions configuration

Loading conditions for a metro vehicle are defined by the loading offset (denoted by $x$ and $y$) and the quantity of the cargoes (denoted by $h$), as illustrated in Fig. 4. For the metro vehicle adopted in this study, the length, width, and height of its inner room are 19 m, 2.8 m, and 2.1 m respectively. Considering the space that the seats occupy and the necessary passage for moving cargoes, we assume the cargoes can be loaded within an oblong area whose length and width are 15 m and 2 m respectively. The maximum height of the cargo is set as 2 m. In the meanwhile, the minimum value of h is set as 0.2 m to guarantee that the vehicle is loaded.

The cargo's center of gravity is represented as a point in Fig. 9, where O$^{\#}$ and O denote the gravity centers of the cargo and vehicle respectively, $M$ denotes the mass of the cargo, $l$ denotes half of the distance between center pivots which is 12.6 m for this metro vehicle. Based on the experience, if the lateral loading offset exceeds 0.2 m, the uneven load distribution will significantly worse the performance of the suspension system. Thus, the maximum value of $y$ is defined as 0.2 m. According to regulations published by Chinese Railways and the Association of American Railroads (AAR) (Chinese Railway, 2006; Transportation Technology Center Inc., 2010), the longitudinal loading offset should follow two basic requirements as: (1) the gravity center of the cargo should be located between the two bogies; (2) the load distributed on either bogie should not exceed half of the maximum static load, which is 21.12 t. Consequently, the limited value of $x_{max}$ (unit: m) can be calculated as:

$$x_{max} = \begin{cases} 6.3 & M < 10.56t \\ \dfrac{10.56 \bullet 12.6}{M} - 6.3 & M \geq 10.56t \end{cases} \tag{9}$$

Because the maximum volume of the cargo is 60 m$^3$ considering the constraint of the vehicle's inner room and the maximum static load is 21.12 t, the minimum density of the cargo can be calculated as (21.12E + 3)/60 = 352 kg/m$^3$ if the vehicle is fully loaded, which is the best condition for improving the transport efficiency and saving the cost. When the mass of the cargo remains constant, lower cargo density will result in higher gravity center that brings with larger moment torque of the gravity on curve tracks. Thus, generally speaking, lower cargo density worsens the running safety of freight trains. For revealing the impact of cargo density, the simulations were conducted with the largest

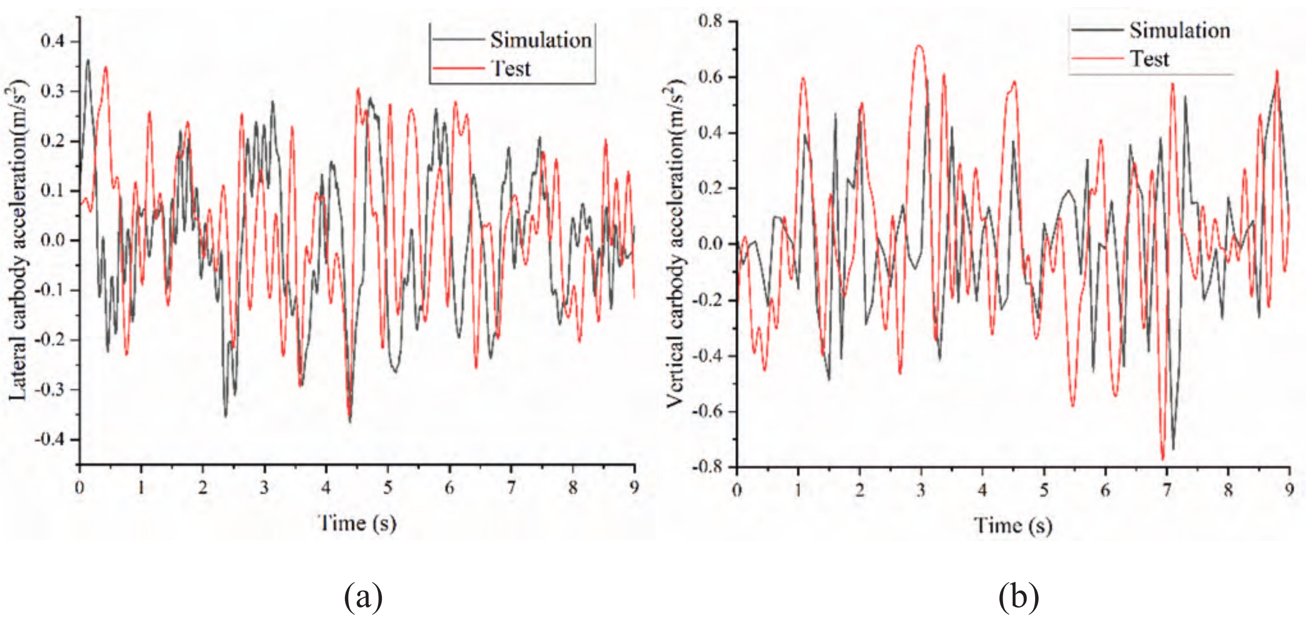


**Fig. 8.** The carbody accelerations: (a) in lateral direction, and (b) in vertical direction.

**Table 5**
Design of running conditions.

| Parameter | Values | | | | |
|---|---|---|---|---|---|
| $R$ (m) | 600 | 900 | 1200 | 1500 | 1800 |
| $v$ (km/h) | 40 | 60 | 80 | 100 | 120 |

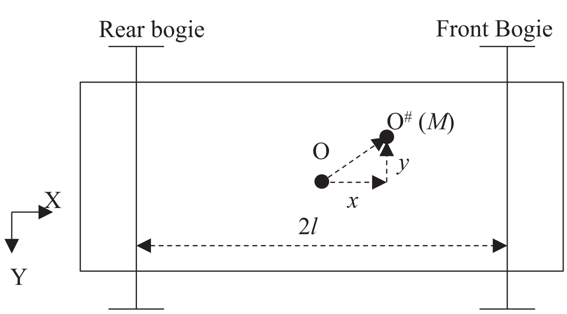


**Fig. 9.** Loading offset of the metro vehicle.

loading offset when the vehicle is half-loaded. To be specific, the cargo mass is 10.56 t, $x$=±6.3 m, $y$=±0.2 m, the cargo density increased from the smallest value of 352 kg/m$^3$ to 704 kg/m$^3$ in increments of 70.4 kg/m$^3$. For evaluating the running performance of the vehicle under the worst condition, the vehicle speed is set as the maximum value of 120 km/h and the curve radius is set as the minimum value of 600 m. The wheel unloading ratio (denoted by UN) is adopted as the safety index because it is significantly affected by the loading offset (Zhang et al., 2021b). The simulation results are illustrated in Fig. 10.

For all investigated ($x$, $y$) pairs, UN gently decreases (or remains nearly flat) as density increases. In other words, the highest UN value always occurs at the minimum density (density = 352 kg/m$^3$). This monotonic trend is consistent across both positive and negative offsets. Therefore, any ($x$, $y$) pair that achieves a low UN under the minimum-density condition will produce equal or lower UN under all higher densities. This ensures that the optimized solution remains safe and effective over the entire practical density range. Moreover, the variation in UN due to density is relatively small compared to the overall magnitude of UN and basically does not alter the ranking of the candidate ($x$, $y$) configurations. Hence, in order to reduce the number of independent variables for the feasibility of large-scale simulations, the cargo density is assumed as its smallest value of 352 kg/m$^3$. This simplification is robust and does not introduce any risk of underestimating UN. According to the assumed density and geometric parameters of the cargo model, Eq. (9) can be derived into Eq. (10) as

$$x_{max} = \begin{cases} 6.3h < 1m \\ \left(\frac{12.6}{h}\right) - 6.3h \geq 1m \end{cases} \tag{10}$$

For better expression, $x^*$ is used to represent the calculation result of $\left(\frac{12.6}{h}\right)$ −6.3. Based on the aforementioned analysis, the loading conditions of the metro vehicle in simulations are listed in Tables 6 and 7, where the positive $x$ means the gravity center of the cargo is closer to the front bogie and the positive $y$ means the cargo is located on the right of the vehicle. Because there should not be loading offset when the vehicle is fully loaded ($h$ = 2), the maximum value of $h$ is designed as 1.8 m in this study.

Experimental studies on bulk cargo displacement showed axle load variations in the range of 1.4 % to 4.9 % (Scherbakov et al., 2023). Such variations, while not entirely negligible, are of a secondary order compared with the wide range listed in Tables 6 and 7. Thus, neglecting the nonlinear sloshing effects caused by loose-stacking packages will not compromise the robustness of the conclusions.

### 3.2. Evaluation of running performance

The running performance of the metro vehicle will be evaluated from the perspective of operation safety and energy efficiency to provide the optimization objectives for cruising speed. The operation safety is evaluated by UN. The energy efficiency can be evaluated through the value of ECMR. As shown in Fig. 11, by means of a PID controller, the traction force will be adjusted in real time to keep the metro vehicle cruising at a constant speed by overcoming the motion resistances such as the wheel-rail contact forces and suspension forces. According to the energy flows of the vehicle system, the ECMR can be calculated as (Zhang et al., 2023b).

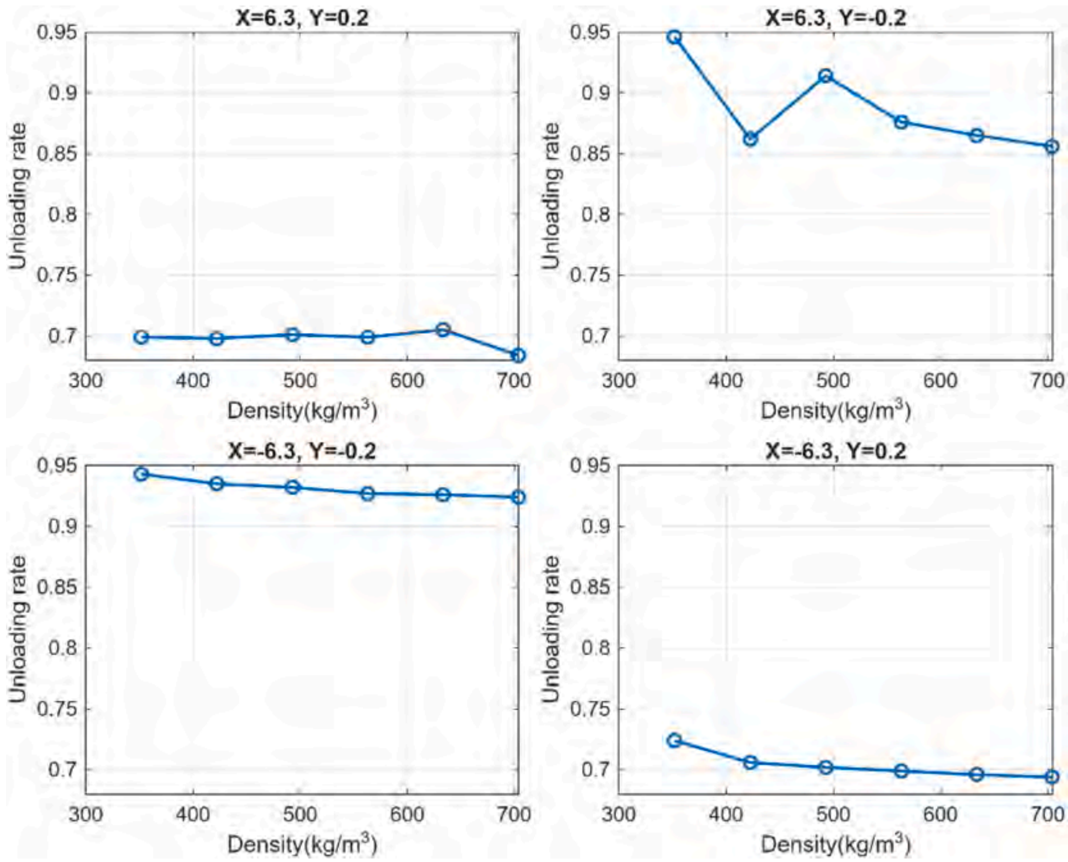


**Fig. 10.** Effects of cargo density on the running safety.

**Table 6**
Load characteristics when the vehicle has not been half-loaded.

| Parameter | Values (m) | | | | |
|---|---|---|---|---|---|
| $h$ | 0.2 | 0.4 | 0.6 | | 0.8 |
| $x$ | −6.3 | −3.15 | 0 | 3.15 | 6.3 |
| $y$ | −0.2 | −0.1 | 0 | 0.1 | 0.2 |

**Table 7**
Load characteristics when the vehicle has been half-loaded.

| Parameter<br>$h$ | Values (m)<br>1 | <br>1.2 | <br>1.4 | <br>1.6 | <br>1.8 |
|---|---|---|---|---|---|
| $x$ | $-x^*$ | $-x^*/2$ | 0 | $x^*/2$ | $x^*$ |
| $y$ | −0.2 | −0.1 | 0 | 0.1 | 0.2 |

$$\text{ECMR} = \int_0^t (F_t v)dt \tag{11}$$

where $F_t$ denotes the traction force, and $t$ denotes the total time required for the vehicle to negotiate the fixed 360 m curved track.

According to the values illustrated in Tables 5, 6, and 7, 5625 simulation cases were performed in total. The input variables contain 5 parameters which can describe the specific working condition: $R$, $v$, $x$, $y$, and $h$. Regarding the curve negotiation process, the maximum absolute value of UN and the calculation result of ECMR based on Eq. (11) are adopted as the output variables.

As an effective technique for visualizing high-dimensional data (Tang et al., 2021; Wu, X. et al., 2025), the parallel coordinate plot (PCP) is employed in this study to present the simulation results. In a PCP, each parallel axis represents a variable, with individual values marked as points along the respective axes. The value of the output variable is encoded in the color of the polyline connecting these points across all axes.

Fig. 12 illustrates the values of UN in the 5625 cases. The PCP enables a preliminary identification of the influence of each input variable on operation safety. Operation safety is most compromised when the vehicle is approximately half-loaded. Improved performance is observed when the cargo is positioned on the left side, near the transversal centerline of the vehicle. Additionally, reducing the curve radius or increasing the cruising speed appears to enhance safety by alleviating cant excess effects. It should be noted, however, that these observations represent general statistical trends. To ensure operation safety in practice, each specific scenario must be accurately evaluated using more advanced techniques.

In contrast, the distribution characteristics of ECMR are less straightforward to interpret. Therefore, the axis arrangement in Fig. 13 is reconfigured to examine ECMR patterns from multiple perspectives. The results clearly indicate that energy consumption decreases as the curve radius increases. Furthermore, positioning the cargo toward the left and rear of the vehicle is associated with higher energy efficiency in a greater number of cases. Both cruising speed and cargo quantity exhibit positive correlations with ECMR.

Although PCP provides intuitive insights into the role of each variable in vehicle performance, the inherent uncertainties in vehicle-track coupled system result in the complex nonlinearity. Especially facing the limited sample data, the machine learning model can be a useful tool for performance prediction (Zhang, Y. et al., 2025; Dandiwala et al., 2024; Singh et al., 2023). Thus, it is necessary to develop precise surrogate models for the accurate and rapid prediction of these indices. Such models are essential to support the optimization of cruising speed in response to specific load characteristics.

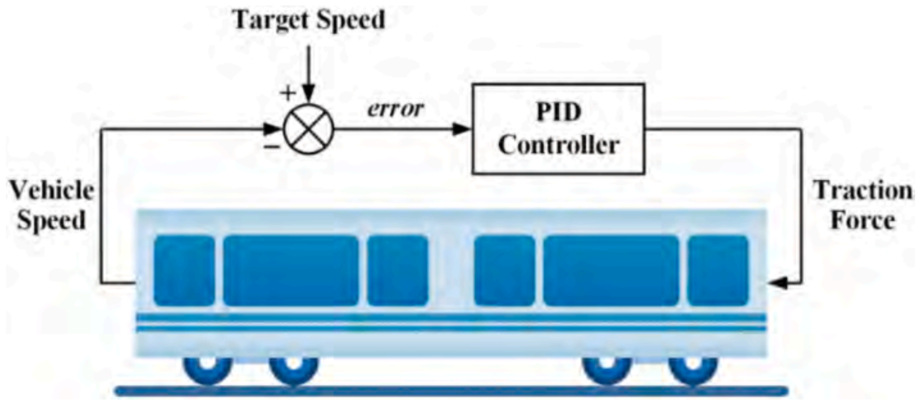


**Fig. 11.** The control of traction force.

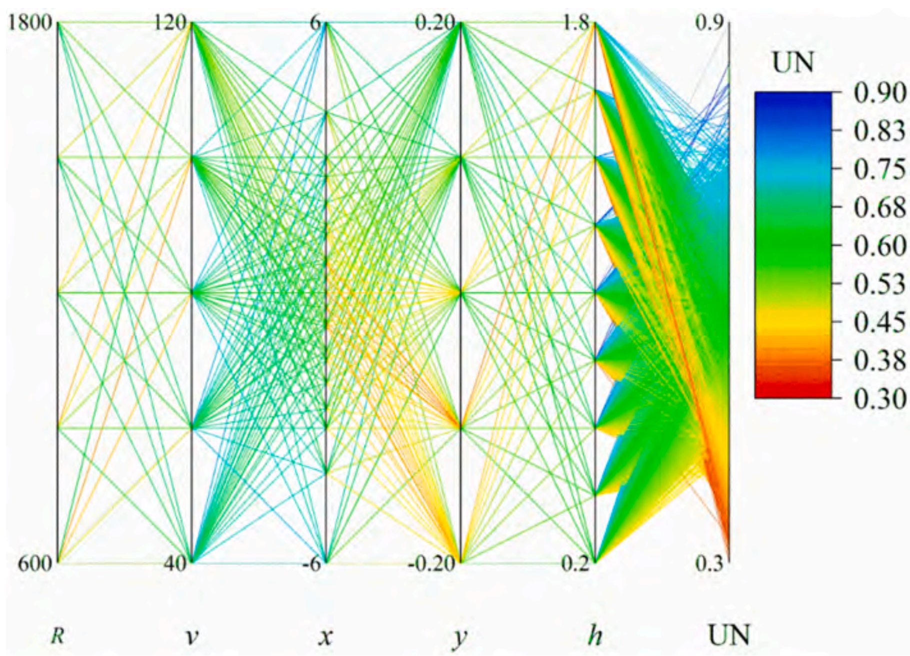


**Fig. 12.** Simulation results of UN.

## 4. Establishment of the surrogate model

The RF algorithm was chosen for its lightweight efficiency in modeling complex, non-linear relationships with minimal data preprocessing. Unlike computationally heavy alternatives, such as deep neural networks or Gaussian process regression, RF provides an optimal balance of robust performance and low computational cost for moderate-sized tabular datasets adopted in this research (5625 samples). It requires minimal hyperparameter tuning, thereby enabling accelerated training and inference times. Additionally, it inherently delivers engineering interpretability via Mean Decrease Impurity, making it an ideal, low-overhead surrogate model.

### *4.1. Parameter tuning*

This study utilized the Scikit-Learn library for all experimental implementations. Model performance was evaluated using the root mean squared error (RMSE) and the coefficient of determination ($R^2$), where a lower RMSE indicates superior accuracy and an $R^2$ value closer to 1.0 signifies a better fit. The dataset was split into 4,500 samples for training and 1,125 for testing, and the training process employed 5-fold cross-validation to ensure robustness. Furthermore, the standard RF architecture was extended by adding a constrained layer prior to the input layer to explicitly encode the feature relationships as defined in Eq. (10).

This section investigates two key hyperparameters: the number of trees and the maximum tree depth. These parameters directly control model complexity. The objective was to train a model that is as simple as possible to facilitate its integration into subsequent optimization simulations.

Fig. 14(a) illustrates the variation in the $R^2$ for the UN regression model with respect to the number of trees, while the maximum depth was fixed at 50. The results indicate that $R^2$ values for both the training and test datasets stabilized with 500 or more trees. Similarly, Fig. 14(b) shows the $R^2$ variation with maximum tree depth for three different ensemble sizes (500, 600, and 700 trees). Model performance stabilized at a maximum depth of 18, irrespective of the number of trees. Consequently, the optimal RF configuration for predicting UN employs 500 trees and a maximum depth of 18. This model achieved an RMSE of 0.0061 (training) and 0.014 (test), and an $R^2$ of 0.9949 (training) and 0.9735 (test).

Fig. 15(a) illustrates the variation in $R^2$ for the ECMR regression model as a function of the number of trees, with the maximum depth fixed at 50. The results show that the $R^2$ values for both the training and

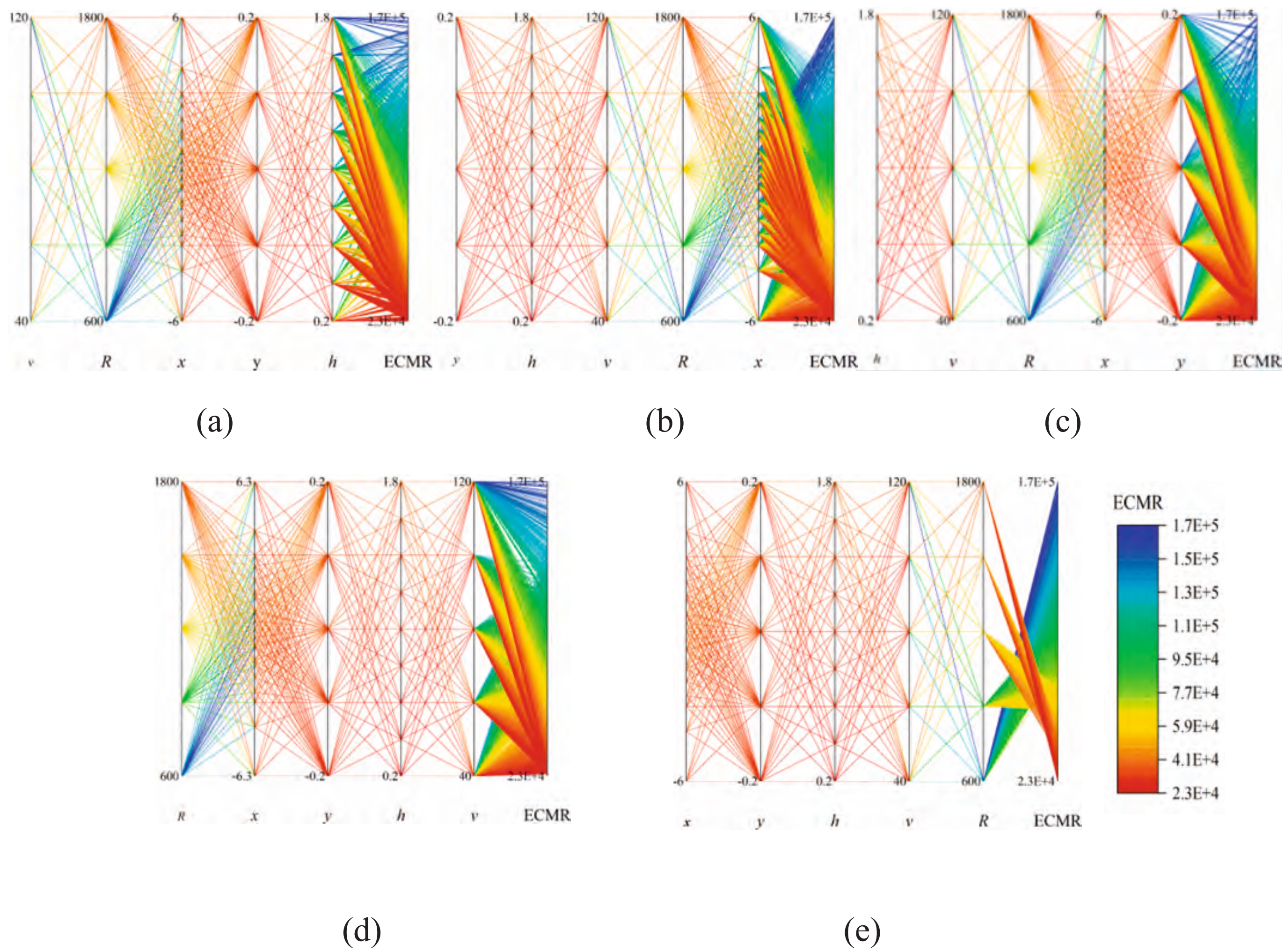


**Fig. 13.** Simulation results of ECMR with different orders of axis.

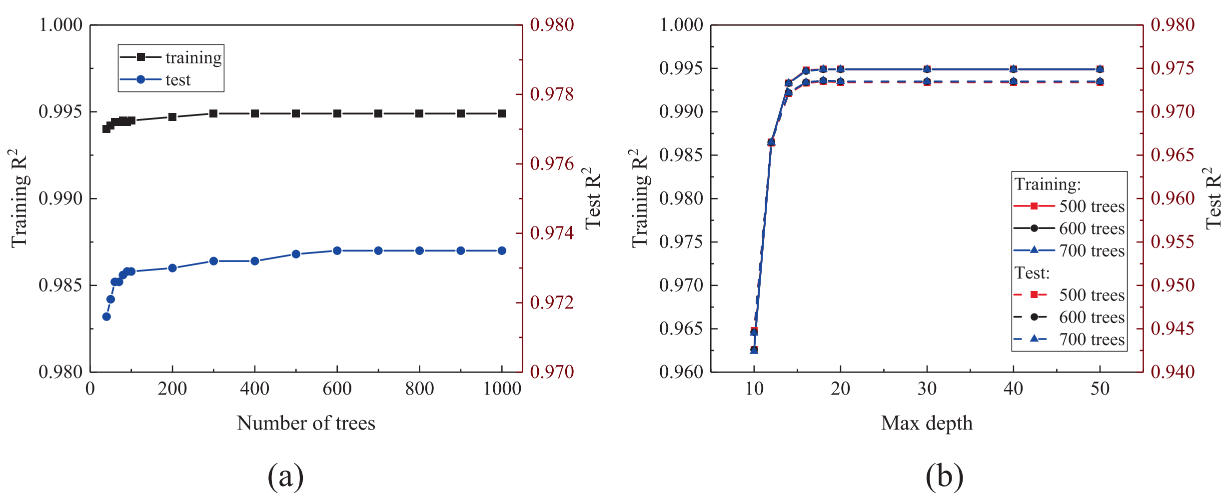


**Fig. 14.** Parameter tuning for RF model for UN: (a) influence of number of trees with max depth fixed at 50, and (b) influence of max depth with given optimal number of trees.

test datasets stabilized when 50 or more trees were used. Due to the minimal variation in $R^2$ observed in Fig. 15(a), the corresponding RMSE values are also superimposed as dashed lines to provide further insight. The RMSE values for both datasets stabilized when 70 or more trees were used.

Similarly, Fig. 15(b) presents the RMSE as a function of the maximum tree depth for three ensemble sizes (60, 70, and 80 trees). The model's performance stabilized at a maximum depth of 13, regardless of the number of trees. Therefore, the optimal RF configuration for ECMR prediction utilizes 70 trees and a maximum depth of 13. This model

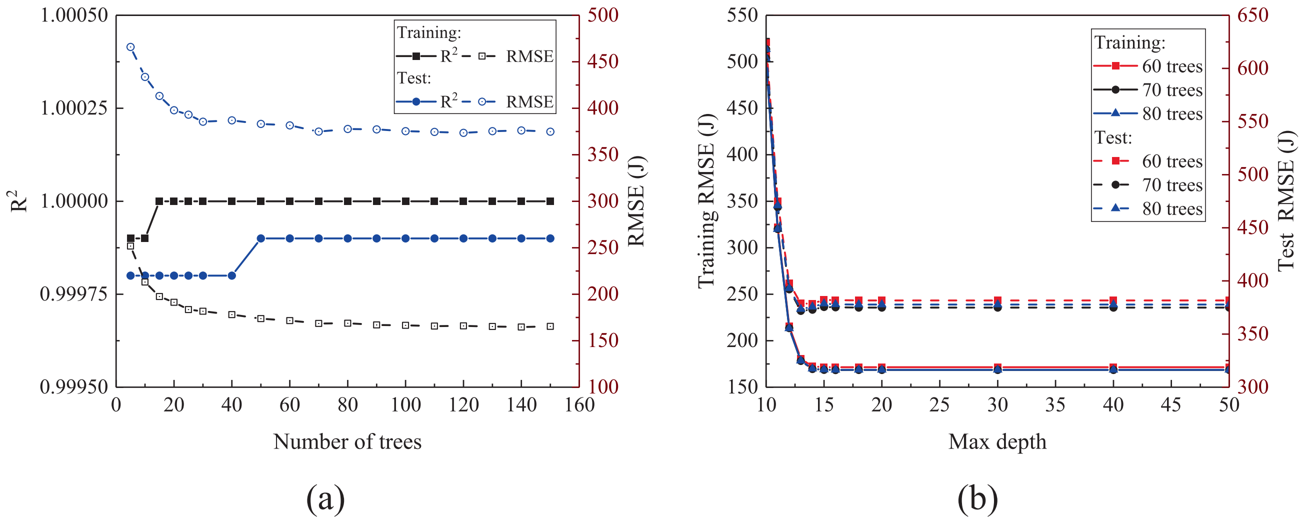


**Fig. 15.** Parameter tuning for RF model for ECMR: (a) influence of number of trees with max depth fixed at 50, and (b) influence of max depth with given optimal number of trees.

achieved an exceptionally high performance, with RMSE values of 178.2 (training) and 371.8 (test), and near-perfect $R^2$ scores of 1.0000 (training) and 0.9999 (test).

### 4.2. Performance of selected RF regression models

This section examines the regression performance of the proposed surrogate models on the test dataset and analyzes feature importance. Fig. 16(a) illustrates the relationship between the predicted and actual UN values, with a superimposed linear fit. The high $R^2$value of 0.9735 indicates a strong linear correlation, confirming the model's predictive accuracy for UN. Furthermore, Fig. 16(b) presents the feature importance, evaluated using the mean decrease impurity (MDI) metric (SCOMET, E., , 2023). The results demonstrate that all five input features contribute to the prediction, with *R* being the most important and *x* the least. Curve radius dominates UN predictions because it directly governs the lateral dynamics of the vehicle during curve negotiation. As the vehicle traverses a curved track, centrifugal force acts on the carbody, generating an overturning moment that redistributes vertical wheel-rail contact forces. On sharp curves, the centrifugal acceleration is larger, causing greater unloading of the inner wheels and consequently a higher wheel unloading ratio.

To interpret the underlying decision logic, a SHAP (Shapley Additive exPlanations) analysis was conducted on the trained UN surrogate model using the testing dataset. The resulting SHAP summary plot, as shown in Fig. 17, illustrates both the marginal contribution and the impact direction of each feature on the model's output.

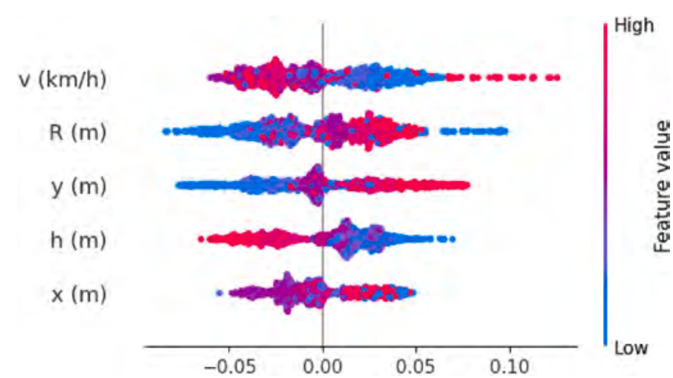


**Fig. 17.** SHAP summary plot for trained UN surrogate model.

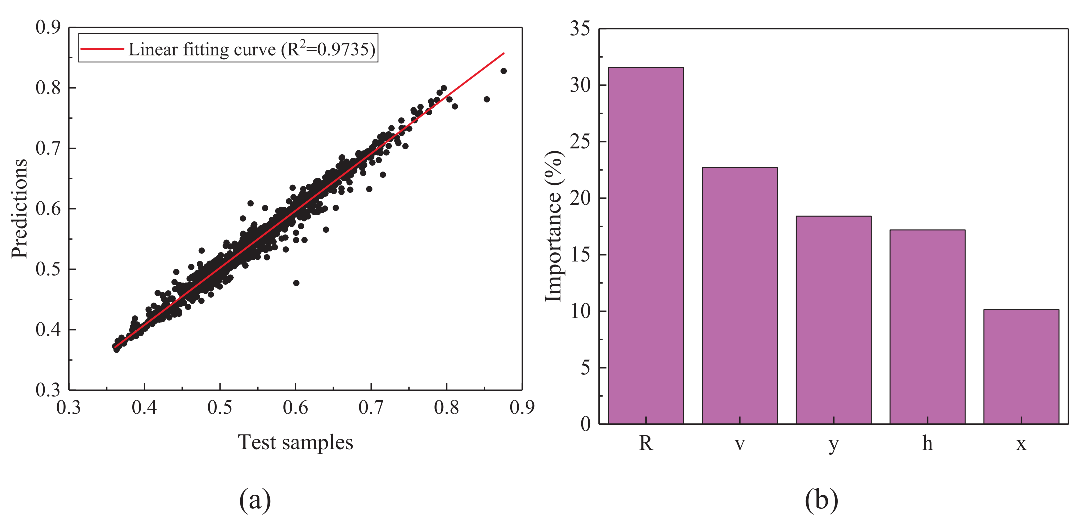


**Fig. 16.** Performance and feature importance of RF model for UN: (a) model prediction performance on test dataset, and (b) importance ranking among the five input features.

Consistent with Fig. 16(b), the features *R*, *v*, *y*, and *h* demonstrate comparable importance in predicting UN, all of which are slightly more influential than the longitudinal offset *x*. Notably, the velocity exhibits a non-linear relationship with UN. Below a specific threshold, *v* is negatively correlated with UN, whereas beyond this threshold, the correlation becomes positive. From a vehicle dynamics perspective, this U-shaped trend captures the balance speed physics during curve negotiation. Similarly, the curve radius displays a non-linear effect, shifting to a positive correlation once it exceeds a certain threshold. Furthermore, the lateral offset *y* and the cargo height *h* exhibit overall positive and negative correlations with UN, respectively. Finally, the longitudinal offset *x* correlates positively with UN after surpassing a certain threshold.

Fig. 18(a) illustrates the relationship between the predicted and actual ECMR values, with a superimposed linear fit. The near-perfect $R^2$value of 0.9999 indicates an exceptionally strong linear correlation, confirming the model's high predictive accuracy for ECMR. Furthermore, the feature importance results in Fig. 18(b) show that *R* dominates the prediction, while *x* the least. Curve radius also dominates ECMR predictions because it is a primary determinant of curve resistance, which is the additional running resistance that a train encounters when negotiating a curved track. This additional resistance increases significantly as curve radius decreases, requiring the traction system to exert greater force to maintain the same cruising speed, thereby consuming more energy.

The SHAP summary plot for trained ECMR surrogate model was shown in Fig. 19. *R* emerges as the most dominant variable, exhibiting a strong negative correlation with ECMR predictions, alongside a broader distribution of SHAP values indicating significant variability across its parameter range. *h* and speed *v* rank as the second and third most influential factors, respectively, each demonstrating a clear positive correlation. The remaining inputs present comparatively marginal importance.

Leave-One-Condition-Out cross-validation experiments were conducted to validate the surrogate model's generalization capability under unseen operating conditions. Given that the fundamental mathematical logic of the RF algorithm is predicated on stepwise weighted averaging, the supplementary validation experiments primarily verified the model's interpolation efficacy within the parameter space boundaries. Initially, a Leave-One-Speed-Out validation was conducted, wherein the data associated with the 60 km/h speed were strictly isolated to serve as an unseen test set. Model training was subsequently performed using the residual dataset (40, 80, 100, and 120 km/h) under consistent hyperparameter settings. The evaluation revealed a satisfactory generalization capacity for the unseen 60 km/h condition: the UN model attained an $R^2$ of 0.8376 (RMSE = 0.0337), while the energy consumption model recorded an $R^2$ of 0.9879 (RMSE = 2967.9949). Following this, a Leave-One-Loading-Condition-Out validation was performed by sequestering all data for a specific height combination (*h* = 1.0). The predictive performance on this reserved dataset also remained favorable, yielding $R^2$ values of 0.9176 and 0.9899, along with RMSE values of 0.0255 and 2950.0438 for the Max_UN and ECMR models, respectively. Cross-validations across other conditions yielded similar accuracy. These outcomes demonstrate that the selected RF model, coupled with the adopted design of experiments (DoE) sampling interval, adequately fulfills the criteria for predicting unseen operational states. In the ensuing optimization stage, the specified curve radii, loading combinations, and the optimized speeds are strictly bound within the training Design Space. Consequently, the RF surrogate model is proven capable of reliably predicting vehicle dynamic behaviors for unprecedented combinations within the trained parametric domain, thereby justifying its deployment in speed optimization tasks.

## 5. Optimization of the cruising speed

### 5.1. Problem description

Based on the analyses presented in **Section 3** and **Section 4**, it is evident that the operation performance of metro vehicles, including both operation safety and energy efficiency, is significantly influenced by the loading and running conditions. Notably, the role that cruising speed plays in vehicle running behavior varies substantially under different loading and track scenarios. For the metro-based ULS, the track conditions of a given line or section are typically predetermined, whereas the cargo loading patterns across stations can be precisely monitored using WIM systems, as described in the **Introduction**. Therefore, adaptively regulating the cruising speed of metro vehicles in response to specific loading and track conditions represents a promising approach to enhancing the operation safety and energy efficiency of the metro-based ULS.

To implement such an adaptive speed optimization strategy, we first partition a metro section into multiple segments based on the consistency of loading and track characteristics, as illustrated in Fig. 20, where *R* denotes the curve radius, *h* denotes the quantity of the cargoes, *x* and *y* denote the loading offset of the cargoes. Subsequently, by leveraging the dependence of vehicle operation performance on cruising speed under diverse loading and track conditions, the cruising speed of each segment is optimized to simultaneously minimize the UN and ECMR. The

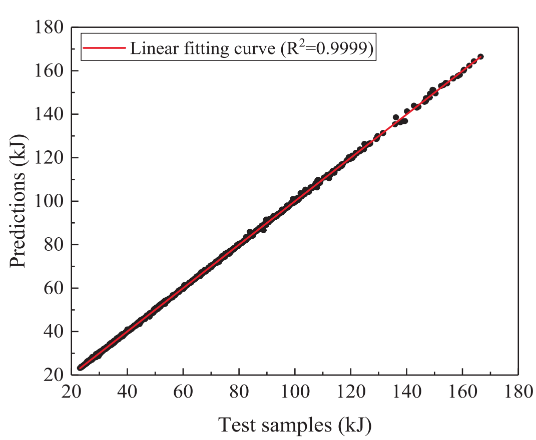


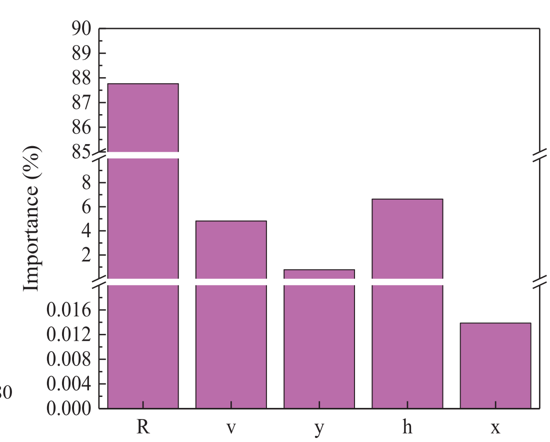


**Fig. 18.** Performance and feature importance of RF model for ECMR: (a) model prediction performance on test dataset, and (b) importance ranking among the five inputs.

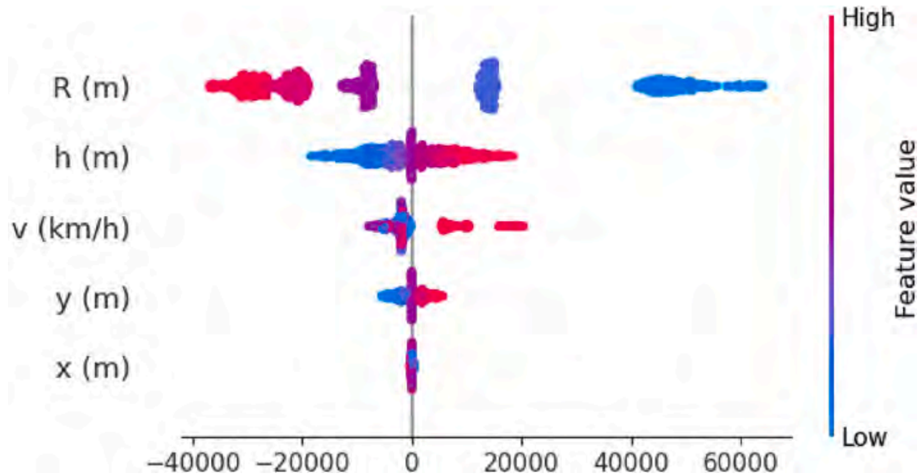


**Fig. 19.** SHAP summary plot for trained ECMR surrogate model.

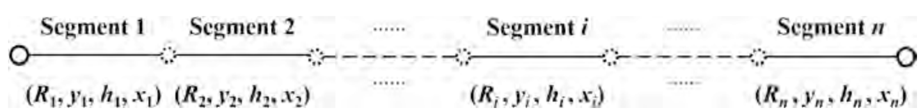


**Fig. 20.** Schematic diagram of a metro section.

resulting optimal cruising speeds are then sequentially applied to the corresponding segments, thereby forming a complete cruising speed profile for the metro section.

### 5.2. Mathematical formulation and solution approach

#### 5.2.1. Bi-objective optimization model

The decision variable of the optimization model is the cruising speed of the considered segment. Two objectives are considered in this model: minimizing the UN to improve operation safety and minimizing the ECMR to reduce energy consumption.

Based on the established surrogate models, the UN and ECMR of a segment can be expressed as

$$f_{UN} = \mathrm{UN}(R, v, y, h, x) \tag{12}$$

$$f_{ECMR} = \mathrm{ECMR}(R, v, y, h, x) \tag{13}$$

where $f_{UN}$ and $f_{ECMR}$ denote the regression functions of the UN and ECMR derived from the surrogate model, respectively, $v$ denotes the cruising speed of the segment, $R$ denotes the curve radius of the track, $h$ denotes the quantity of the cargoes, $x$ and $y$ denote the loading offset of the cargoes.

Thus, the objective function of the optimization problem can be formulated as

$$Min f = (f_{UN}, f_{ECMR}) \tag{14}$$

To ensure practical operation, the cruising speed is constrained by

$$v_{min} \leq v \leq v_{max} \tag{15}$$

where $v_{min}$ and $v_{max}$ denote the lower and upper speed limits, respectively.

Furthermore, to satisfy operational efficiency requirements, the running time of each segment is constrained by

$$\frac{L}{v} \leq T_{max} \tag{16}$$

where $L$ denotes the length of the segment, $T_{max}$ denotes the maximum allowable running time for the segment.

#### 5.2.2. Adaptive evolutionary algorithm

In order to tackle multi-objective models, various evolutionary algorithms have been developed to obtain the Pareto fronts (Guo et al., 2026). Among these, dominance-based algorithms such as NSGA-II (Deb et al., 2002) prioritize Pareto-dominance relationships to guide population evolution, while decomposition-based methods such as MOEA/D (Zhang & Li, 2007) transform multi-objective problems into a series of scalar subproblems. Indicator-based algorithms, by contrast, employ performance indicators such as the hypervolume to drive the search toward well-distributed Pareto fronts (Bader & Zitzler, 2011). In addition, given that fitness evaluations in many engineering applications rely on time-consuming simulations or physical experiments, surrogate-assisted evolutionary algorithms (SAEAs) have been developed to replace costly evaluations with computationally efficient surrogate models. Representative SAEAs such as SAMOEA-TL2M (Liu et al., 2025) and SADE-KT (Liu et al., 2023) demonstrate that embedding surrogate models within the evolutionary framework can improve search efficiency and solution quality under limited evaluation budgets. The surrogate modeling framework embedded in these algorithms offers a principled means of approximating expensive objective functions.

The optimization problem proposed in this study similarly relies on surrogate models to evaluate the objectives, and presents two major challenges. First, the objective functions are derived from surrogate models, which may lead to irregular, discontinuous, or degenerate Pareto fronts. Second, due to the black-box nature of these objective functions, no gradient information is available.

To overcome these problems, this study employs the adaptive reference point-based multi-objective evolutionary algorithm (AR-MOEA) to solve the proposed model. AR-MOEA is an indicator-based multi-objective evolutionary algorithm characterized by its reference point adaptation mechanism, thereby enabling automatic adjustment to Pareto fronts of various shapes (Tian et al., 2017). This allows the algorithm to effectively approximate both regular and irregular Pareto fronts without requiring prior knowledge of the front shape (Cheng et al., 2019; Zhang, X. et al., 2025). Besides, AR-MOEA does not require derivative information and relies solely on objective function evaluations (Long et al., 2022), rendering it ideal for regression-model-driven objectives.

The flow of AR-MOEA can be summarized in three main phases:

*Step 1.* Initialization.
***Step 1.1.*** Generate the population set *P* and predefine a set of uniformly distributed reference points *Z*.
***Step 1.2.*** Initialize the archive *A* to the population. Set the adapted reference point set *Z*' as a copy of the uniform set *Z*.
*Step 2.* Main Evolutionary Loop.
***Step 2.1.*** Use binary tournament strategy to select mating pool *P*' from population *P*. Apply genetic operators (e.g., crossover, mutation) to the mating pool *P*' and generate offspring *Q*.
***Step 2.2.*** Update the archive *A* by incorporating the new offspring *Q* and removing any dominated or duplicate solutions.
***Step 2.3.*** Adapt the reference point set *Z*' by combining the initial uniform points *Z* with points from the archive *A*.
***Step 2.4.*** Combine the parent population and the offspring to form a candidate pool.
***Step 2.5.*** Select the best solutions through a two-stage process: Perform non-dominated sorting to prioritize solutions based on convergence; Calculate the enhanced inverted generational distance indicator and select those that optimize diversity and spread.
*Step 3.* Termination check.
***Step 3.1.*** The loop terminates when the maximum number of generations or another stopping criterion is met.
***Step 3.2.*** Output the final population *P* as an approximation of the Pareto front.

The complete online optimization procedure, integrating the trained Random Forest surrogate models with the AR-MOEA algorithm, is summarized in Algorithm 1. Given the trained RF surrogate models together with the current track and loading conditions, the AR-MOEA algorithm is employed to optimize the cruising speed of an individual metro segment. Candidate cruising speeds are first initialized within the prescribed speed limits and then evaluated using the RF surrogate models to obtain the corresponding UN and ECMR values. Through iterative crossover, mutation, reference-point updating, and environmental selection, the Pareto-optimal solution set is gradually obtained. Finally, a representative solution is selected from the Pareto front as the cruising speed control target for the current segment.

Algorithm 1: Online Data-Driven Multi-Objective Optimization for Train Speed.

**Input:** Trained Random Forest models: $\mathrm{RF_{UN}}(\cdot)$, $\mathrm{RF_{ECMR}}(\cdot)$
Real-time state variables: $\mathrm{R, x, y, h}$
Algorithm parameters: Population size $\mathrm{N}$, Max generations $\mathrm{G_{max}}$
Decision space bounds: $[\mathrm{v_{min}}, \mathrm{v_{max}}]$
**Output:**Optimal speed control target: $\mathrm{v^*}$
1: **while** train is in operation **do**
2:Read current state parameters $(\mathrm{R, x, y, h})$ from system
3:Initialize $\mathrm{P_0} \leftarrow$ randomly sample N velocities $\mathrm{v_i} \in [\mathrm{v_{min}}, \mathrm{v_{max}}]$
4:$\mathrm{g} \leftarrow 0$
5:while $\mathrm{g} < \mathrm{G_{max}}$ do
6:for each individual $\mathrm{v_i} \in \mathrm{P_g}$ do
7:$\mathrm{X_i} \leftarrow [\mathrm{R, x, y, v_i, h}]$
8:$\mathrm{UN_i} \leftarrow \mathrm{RF_{UN}}(\mathrm{X_i})$, $\mathrm{ECMR_i} \leftarrow \mathrm{RF_{ECMR}}(\mathrm{X_i})$
9:$\mathrm{F}(\mathrm{v_i}) \leftarrow (\mathrm{UN_i}, \mathrm{ECMR_i})$
10: **end for**
11:$\mathrm{Q_g}\leftarrow$Generateoffspring from$\mathrm{P_g}$viaCrossover&Mutation
12:Evaluate fitness $\mathrm{F}(\mathrm{Q_g})$ using $\mathrm{RF_{UN}}$ and $\mathrm{RF_{ECMR}}$
13:$\mathrm{R_g} \leftarrow \mathrm{P_g} \cup \mathrm{Q_g}$
14:Update Auto-Reference points based on non-dominated solutions in $\mathrm{R_g}$
15:$\mathrm{P_{g+1}} \leftarrow$ Select N individuals from $\mathrm{R_g}$ via reference-point criteria
16:$\mathrm{g} \leftarrow \mathrm{g}+1$
17: **end while**
18:PF $\leftarrow$ Extract the Pareto Front (non-dominated set) from $\mathrm{P_{G_{max}}}$
19:$\mathrm{v^*} \leftarrow$ Select the best compromise solution from PF
20:Output and apply $\mathrm{v^*}$to the train control system
21: **end while**

### 5.3. Case study

#### 5.3.1. Experimental design

To illustrate the effectiveness of the proposed approach, a representative numerical metro section is constructed based on realistic design ranges to demonstrate the applicability of the proposed optimization framework under heterogeneous track and loading conditions. This metro section is partitioned into ten distinct segments according to variations in track curvature and cargo distribution patterns. Specifically, the curve radii are chosen within the operating range considered in Section 3.1.1, while the loading parameters are selected within the feasible loading domain defined in Section 3.1.2, including the limits on cargo height, lateral loading offset, and longitudinal loading offset. These ranges are defined to reflect the operational characteristics of metro-based ULS. The specific track and loading parameters for each segment are listed in Table 8.

The lower and upper speed limits of the metro vehicle are set at 40 km/h and 120 km/h, respectively, and each segment is assumed to have a length of 360 m. Under the prescribed speed limits, the corresponding running time of a segment ranges from approximately 10.8 s to 32.4 s. To represent a practical operational requirement while allowing sufficient flexibility for speed optimization, the allowable running time for each segment is set to 21.6 s, corresponding to the midpoint of the feasible running-time interval.

#### 5.3.2. Algorithm settings and performance analysis

The performance of AR-MOEA is influenced by several algorithmic parameters, including the population size, the maximum number of iterations, the crossover probability, the mutation probability, and the reference-point generation strategy (Tian et al., 2017). Among these, the population size and the maximum number of iterations primarily determine the search capability and computational budget of the algorithm (Deb et al., 2002), whereas the crossover probability, mutation probability, and reference-point settings are standard algorithmic parameters with well-established default values (Chugh et al., 2016). Therefore, the sensitivity analysis in this study focuses on the population size and the maximum number of iterations, while the remaining parameters follow the default settings recommended in the original AR-MOEA study (Tian et al., 2017).

All numerical experiments were performed on a PC equipped with an AMD Ryzen 9 9950X processor (4.30 GHz) and 192 GB of RAM. The simulations were conducted using MATLAB R2020b.

To determine an appropriate population size and to identify a sufficient number of iterations for convergence, a sensitivity analysis was conducted by varying the population size ($N = 20, 50, 100$), while fixing the number of iterations at 50, with 10 independent runs performed for each setting. Fig. 21 presents the average hypervolume (HV) convergence curves for Segment 1 as a representative example. The HV indicator measures the volume of the objective space dominated by the obtained Pareto front, where a larger HV value indicates better convergence and diversity of the solution set (Zitzler et al., 2003).

**Table 8**
Track and loading parameters for each metro segment.

| Segment | *R* (m) | *y* (m) | *h* (m) | *x* (m) |
|---|---|---|---|---|
| 1 | 600 | −0.17 | 1.62 | −1.4 |
| 2 | 1600 | 0 | 1.22 | 0 |
| 3 | 1700 | 0.16 | 1.47 | 1.25 |
| 4 | 1000 | 0.1 | 0.73 | −0.54 |
| 5 | 700 | 0 | 1.54 | −1.85 |
| 6 | 1800 | −0.12 | 0.6 | 5.19 |
| 7 | 1000 | −0.2 | 0.92 | −6.3 |
| 8 | 600 | 0.2 | 1.8 | 0.4 |
| 9 | 1600 | 0.15 | 0.25 | 3.84 |
| 10 | 1200 | −0.18 | 1.6 | −1.58 |

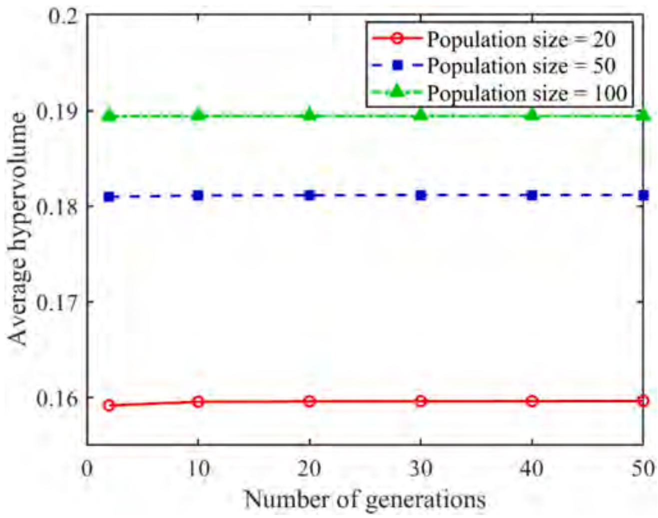


**Fig. 21.** Average hypervolume convergence curves of AR-MOEA for Segment 1 under different population sizes over 10 independent runs.

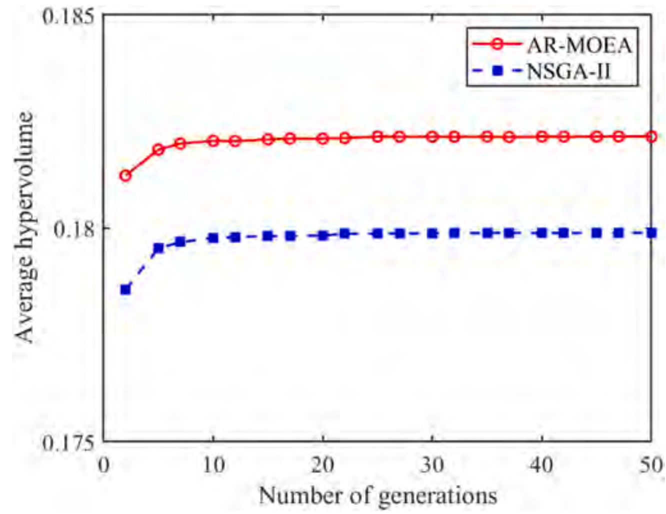


**Fig. 22.** Comparison of the average hypervolume convergence curves of AR-MOEA and NSGA-II over 10 independent runs.

As shown in Fig. 21, the average HV values rapidly stabilize during the early generations for all population sizes and remain nearly unchanged thereafter, indicating that 50 generations are sufficient to achieve convergence for the proposed optimization problem. Increasing the population size from 20 to 50 leads to a noticeable improvement in the final HV value, whereas a further increase to 100 yields only a marginal improvement while incurring a substantially higher computational cost. Therefore, a population size of 50 and a maximum number of generations of 50 are adopted in the subsequent optimization, providing a good compromise between solution quality and computational efficiency.

Based on the above analysis, the AR-MOEA is configured with the parameter settings summarized in Table 9.

To further evaluate the performance of AR-MOEA, a comparative analysis with NSGA-II was conducted on Segment 1. Both algorithms were independently executed 10 times with different random seeds under identical parameter settings. Fig. 22 presents the average HV convergence curves obtained from these independent runs.

As shown in Fig. 22, both algorithms rapidly converge during the early generations, demonstrating that the proposed optimization problem can be efficiently solved by evolutionary algorithms. Nevertheless, AR-MOEA consistently achieves higher HV values than NSGA-II throughout the optimization process. This trend reflects stronger convergence performance and a better balance between convergence and solution diversity.

In terms of computational efficiency, the average execution time of AR-MOEA over the 10 independent runs was 4.9 s, compared with 5.3 s for NSGA-II, corresponding to a reduction of approximately 7.5 % in computational time. Together with the consistently higher HV values, these results indicate that AR-MOEA provides better solution quality while requiring less computational effort, making it a more suitable optimization algorithm for the proposed optimization problem.

**Table 9**
Parameter configuration of the AR-MOEA.

| Parameter | Value |
|---|---|
| Population size | 50 |
| Maximum number of iterations | 50 |
| Reference point | Das and Dennis's approach |
| Crossover probability | 1 |
| Mutation probability | 0.1 |

### 5.3.3. *Optimization results*

To illustrate the optimization results of the proposed framework, Segment 1 is taken as a representative example. Fig. 23 presents the Pareto front obtained for this segment. The Pareto front consists of a set of non-dominated solutions, revealing the trade-off between operational safety and energy efficiency.

Since the obtained Pareto front contains a set of non-dominated solutions rather than a unique optimum, a multi-criteria decision-making method is required to identify representative solutions for practical engineering applications. In this study, the technique for order preference by similarity to ideal solution (TOPSIS) is employed to rank the obtained Pareto solutions. TOPSIS evaluates each Pareto solution according to its relative distance to the ideal and anti-ideal solutions. A solution closer to the ideal solution and farther from the anti-ideal solution receives a higher ranking (Behzadian et al., 2012).

To represent different operational priorities, two extreme weighting scenarios are considered. When the objective weight is assigned as (1,0), priority is given entirely to operational safety, and the highest-ranked solution is referred to as the safety-optimal solution. Conversely, when the objective weight is (0,1), priority is given entirely to energy efficiency, and the highest-ranked solution is referred to as the energy-optimal solution.

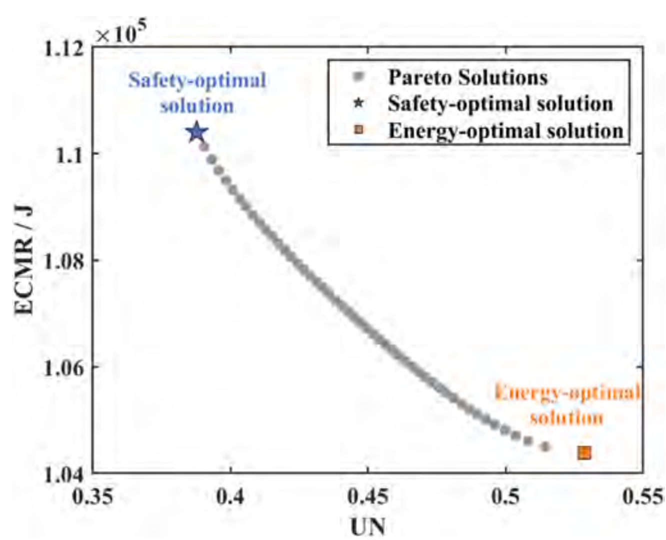


**Fig. 23.** Pareto front for Segment 1 with the representative solutions.

As shown in Fig. 23, the safety-optimal solution is highlighted by the blue star, whereas the energy-optimal solution is indicated by the orange square. These two representative solutions provide practical operating strategies for safety-oriented and energy-oriented decision making, respectively.

After determining the representative solutions for each segment, two section-level cruising speed profiles are constructed. The safety-oriented cruising speed profile is obtained by selecting the safety-optimal solution for every segment, while the energy-oriented cruising speed profile is formed by selecting the energy-optimal solution for every segment. The overall operation safety of the section is evaluated by the maximum UN among all segments, whereas the total energy consumption is calculated as the sum of the ECMR values of all segments.

To evaluate the effectiveness of the proposed optimization strategy, four uniform-speed operation scenarios (60, 80, 100, and 120 km/h) are adopted as benchmark cases. These benchmark speeds satisfy the running-time constraint imposed on each segment. The operation safety and energy consumption obtained from the two optimized cruising speed profiles are compared with those of the benchmark scenarios.

Fig. 24 presents the maximum percentage reductions in UN and ECMR achieved by the optimized cruising speed profiles relative to the benchmark operations. As can be observed, the proposed optimization strategy consistently improves either operation safety or energy efficiency compared with all uniform-speed benchmarks. Relative to the 120 km/h benchmark, which represents the most demanding operating condition, the safety-oriented cruising speed profile reduces the section UN by 23.51 %, while the energy-oriented cruising speed profile reduces the total ECMR by 20.75 %. Even when compared with the more conservative benchmark speeds of 60–100 km/h, noticeable improvements are still achieved, with UN reductions ranging from 5.45 % to 12.36 % and ECMR reductions ranging from 0.99 % to 3.46 %. These results demonstrate that adaptively selecting cruising speeds according to the track and loading conditions of individual segments can substantially enhance both operation safety and energy efficiency at the section level.

Fig. 25 illustrates the Pareto-optimal cruising speeds obtained for all metro segments. It can be observed that the optimal cruising speed varies considerably among different segments owing to the combined effects of track geometry and loading conditions. Segments with tighter curves or more unfavorable loading conditions generally require lower cruising speeds to maintain operational safety, whereas segments with larger curve radii and more balanced loading conditions permit higher cruising speeds while preserving energy efficiency. For example, Segment 7 ($R$ = 1000 m, $y$ = -0.2 m, $h$ = 0.92 m, $x$ = -6.3 m) exhibits relatively low Pareto-optimal cruising speeds because of the combined influence of moderate curvature and severe loading imbalance. In contrast, Segment 3 ($R$ = 1700 m, $y$ = 0.16 m, $h$ = 1.47 m, $x$ = 1.25 m) consistently allows higher cruising speeds owing to its gentle curvature and favorable loading conditions.

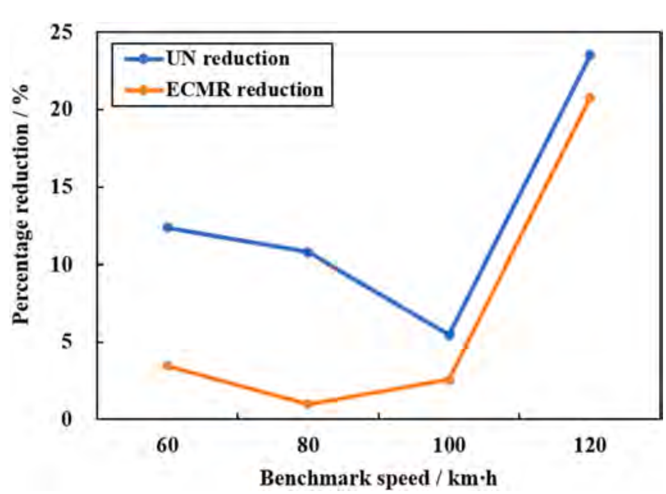

**Fig. 24.** Percentage reductions in section-level UN and ECMR under the proposed optimization framework relative to the uniform-speed benchmarks.

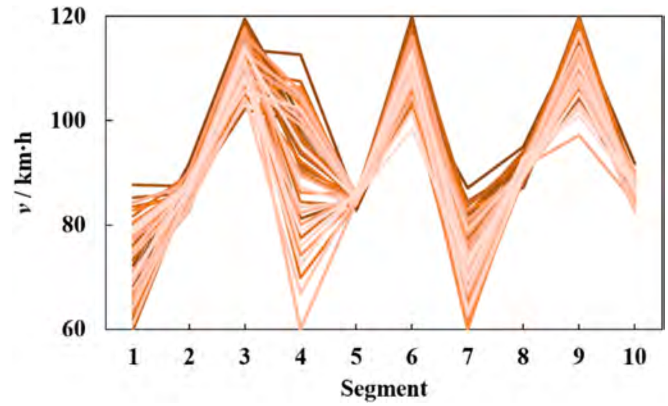

**Fig. 25.** Pareto-optimal cruising speed distributions for different segments.

To further evaluate the effectiveness of the proposed bi-objective optimization framework, an additional rule-based speed control strategy is considered. Since lateral loading offset has a direct influence on vehicle running safety, a speed-limiting rule is established according to the lateral loading offset of each segment. The corresponding speed-limiting rules are summarized in Table 10. Four rule-based benchmark cases are then generated by applying these rules to the uniform-speed benchmarks (60, 80, 100, and 120 km/h).

Fig. 26 compares the percentage reductions in section-level UN and ECMR achieved by the proposed optimization framework relative to the rule-based benchmark strategy. Compared with the rule-based operation, the proposed optimization framework consistently provides better performance under all benchmark speeds. The section-level UN is reduced by 10.76 %-12.36 %, while the total ECMR is reduced by 1.87 %-7.38 %. These results indicate that, although the rule-based strategy improves operation safety by applying predefined speed limits, it cannot simultaneously account for the combined influences of track geometry and cargo loading conditions. In contrast, the proposed optimization framework adaptively determines the cruising speed for each segment based on both track and loading characteristics, thereby achieving a better balance between operation safety and energy efficiency.

The optimization results presented above indicate that the adaptive adjustment of cruising speeds in response to track and loading conditions can effectively improve the operation safety and energy efficiency of metro-based ULS. Moreover, the obtained Pareto optimal solutions offer substantial operational flexibility, enabling system operators to select speed profiles aligned with specific performance priorities. For scenarios where safety is paramount, the safety-optimal solution can be selected, while energy-efficient operations can be achieved by choosing the energy-optimal solution.

## 6. Conclusions

This study proposes a novel optimization framework for determining the cruising speed of metro vehicles in the metro-based ULS, with the aim of simultaneously enhancing operation safety and energy efficiency under vehicle-cargo coupling effects. Taking into account the variation in the carbody's mass properties due to cargo loading, the dynamic

**Table 10**
Rule-based cruising speed limits according to lateral loading offset.

| Lateral loading offset $y$ (m) | Maximum cruising speed (km/h) |
|---|---|
| $y < 0.10$ | No speed reduction |
| $0.10 \leq y < 0.15$ | 100 |
| $0.15 \leq y < 0.2$ | 80 |
| $y \geq 0.2$ | 60 |

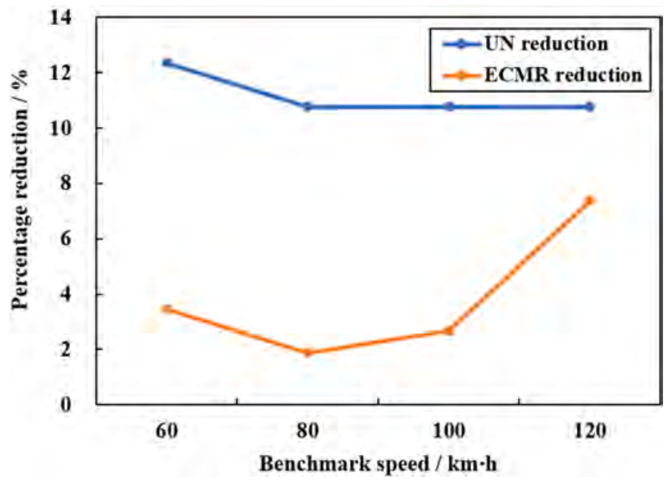


**Fig. 26.** Percentage reductions in section-level UN and ECMR under the proposed optimization framework relative to the rule-based benchmarks.

equations of the loaded carbody are derived to construct the MBD model of a B-type metro vehicle, which is validated through in-situ testing on Chengdu Metro Line 1. A total of 5625 MBD simulations are conducted under designed working conditions covering potential variations in loading offset, cargo quantity, curve radius, and cruising speed within feasible limits. The simulation results elucidate the influence of working conditions on vehicle running performance and serve as the basis for developing the surrogate model using the RF algorithm to predict vehicle performance based on input features related to load characteristics and running conditions. For predefined segments of a metro section, a bi-objective optimization model is formulated to optimize the cruising speed, with safety and energy efficiency indices evaluated via the surrogate model. The optimization model is solved using AR-MOEA, yielding a Pareto front of cruising speeds. A case study confirms the superiority of the proposed framework.

The following insights from this study contribute to the sustainable development of metro-based ULS:

(1) The relationship between working conditions and metro vehicle running performance is complex and nonlinear. Nevertheless, several general conclusions can be drawn from the MBD simulation results. To improve operation safety, it is preferable to avoid half-load conditions. The cargo should be located on the outer side of the vehicle, and the cruising speed should be high for mitigating the impact of cant excess. In contrast, while outer side cargo placement also benefits energy efficiency, higher speeds lead to increased ECMR. Given the conflicting influence of cruising speed on operation safety and energy efficiency, a bi-objective optimization approach is essential.

(2) The RF-based surrogate model accurately predicts metro vehicle running performance under any working condition. Feature importance analysis reveals that curve radius is the most influential factor. Therefore, cruising speed should be optimized not only according to load characteristics but also in response to specific track curvature.

(3) AR-MOEA proves effective for solving the developed bi-objective optimization model, particularly given its suitability for regression-model-driven objectives. The case study shows that adjusting segment-specific cruising speeds according to track and loading conditions can significantly improve both operation safety and energy efficiency. Compared to a uniform speed profile, the proposed optimization strategy reduces the maximum wheel unloading ratio by up to 23.51 % and ECMR by up to 20.75 %.

(4) The proposed AI-driven optimization framework demonstrates that intelligent decision pipelines, combining surrogate learning, evolutionary optimization, and real-time sensing, can effectively address complex railway optimization problems where traditional physical models alone are insufficient.

This study already incorporates five influencing factors (i.e., longitudinal and lateral loading offsets, cargo quantity, curve radius, and cruising speed), resulting in substantial computational demands. To avoid excessive computation, the cargo model assumes vertical uniformity to estimate the height of the carbody's center of gravity based on cargo quantity. Future work will focus on developing a WIM algorithm to accurately determine the vertical position of the center of gravity using WIM data, thereby further refining the accuracy of the MBD vehicle model. The complex coupled simulation approaches (e.g. DEM-MBD co-simulation) could be adopted to take the nonlinear sloshing effects caused by loose stacking into consideration. The practical implementation challenges should also be addressed, including real-time communication with WIM systems for seamless load data transmission and integration of the proposed optimization engine with existing Automatic Train Operation (ATO) and signaling systems. More in-situ tests will be carried out in various working conditions to validate the effectiveness of the proposed methodology.

## Declaration of competing interest

The authors declare that they have no known competing financial interests or personal relationships that could have appeared to influence the work reported in this paper.

## Acknowledgements

This research was supported by the National Natural Science Foundation of China [grant number 52408475].The authors would also like to appreciate the funding supported by European Union's Horizon Europe research and innovation programme for Marie Skłodowska-Curie Actions under Grant TEESFtrain [grant number 101198179].

## Data availability

Data will be made available on request.

## References

*Chinese Railway*, (2006).
Ahmad, S., Wu, Q., Bernal, E., Spiryagin, M., Cole, C., & Buckley, R. (2025). Multibody dynamic analysis of vibrational and frictional energy for railway freight wagons under different track irregularities and curve radii. *Mechanism and Machine Theory, 213*, Article 106076.
Allotta, B., D'Adamio, P., Marini, L., Meli, E., Pugi, L., & Rindi, A. (2015). A new strategy for dynamic weighing in motion of railway vehicles. *IEEE T. Intell. Transp., 16*, 3520–3533.
An, N., Yang, K., Chen, Y., & Yang, L. (2024). Wasserstein distributionally robust optimization for train operation and freight assignment in a metro-based underground logistics system. *Computers and Industrial Engineering, 192*, Article 110228.
Bader, J., & Zitzler, E. (2011). HypE: An algorithm for fast hypervolume-based many-objective optimization. *Evolutionary Computation, 19*, 45–76.
Behiri, W., Belmokhtar-Berraf, S., & Chu, C. (2018). Urban freight transport using passenger rail network: Scientific issues and quantitative analysis. *Transportation Research Part E: Logistics and Transportation Review, 115*, 227–245.
Behzadian, M., Otaghsara, S. K., Yazdani, M., & Ignatius, J. (2012). A state-of the-art survey of TOPSIS applications. *Expert Systems with Applications, 39*, 13051–13069.
Bustos, A., Rubio, H., Castejon, C., & Garcia-Prada, J. C. (2025). Effect of the secondary suspension and intercar links on the performance of a high-speed train. *Mechanism and Machine Theory, 215*, Article 106167.
Chen, H., & Wan, Z. (2023). Characteristic analysis of chengdu metro line 7 track irregularity spectrum. *Urban Mass Transit, 7*, 1–6.
Chen, Z., Hu, W., Xu, Y., Dong, J., Yang, K., & Ren, R. (2023). Exploring decision-making mechanisms for the metro-based underground logistics system network expansion: An example of Beijing. *Tunn. Undergr. Sp. Tech., 139*, Article 105240.
Chen, Z., Li, S., & Yang, L. (2023). Hierarchical optimal control framework to automatic train regulation combined with energy-efficient speed trajectory calculation in metro lines. *Transportation Research Part C: Emerging Technologies, 149*, Article 104059.
Cheng, F., Fu, G., Zhang, X., & Qiu, J. (2019). Multi-objective evolutionary algorithm for optimizing the partial area under the ROC curve. *Knowledge-Based Systems, 170*, 61–69.
Chugh, T., Jin, Y., Miettinen, K., Hakanen, J., & Sindhya, K. (2016). A surrogate-assisted reference vector guided evolutionary algorithm for computationally expensive many-objective optimization. *IEEE T. Evolut. Comput., 22*, 129–142.

Coulombel, N., Dablanc, L., Gardrat, M., & Koning, M. (2018). The environmental social cost of urban road freight: Evidence from the Paris region. *Transportation Research Part D: Transport and Environment, 63*, 514–532.

D'Adamio, P., Marini, L., Meli, E., Pugi, L., & Rindi, A. (2016). Development of a dynamical weigh in motion system for railway applications. *Meccanica, 51*, 2509–2533.

Dandiwala, A., Chakraborty, B., & Chakravarty, D. (2024). An artificial neural network-based integrated tilt control system for narrow electric three-wheelers. *Expert Systems with Applications, 238*, Article 121970.

Deb, K., Pratap, A., Agarwal, S., & Meyarivan, T. (2002). A fast and elitist multiobjective genetic algorithm: NSGA-II. *IEEE T. Evolut. Comput., 6*, 182–197.

Di, Z., Yang, L., Shi, J., Zhou, H., Yang, K., & Gao, Z. (2022). Joint optimization of carriage arrangement and flow control in a metro-based underground logistics system. *Transportation Research Part B: Methodological, 159*, 1–23.

FENG, M., WU, K., LU, S., 2022. A fast-solved model for energy-efficient train control based on convex optimization. arXiv preprint arXiv:2201.10731.

Guo, J., Qin, Y., Wu, C. H., & Chen, Z. (2026). Multi-objective optimization of multimodal logistics paths: A decomposition-based approach for coordinating trucks and UAVs within the cyber-physical internet framework. *International Journal of Logistics Research and Applications*, 1–29.

Guo, J., Wang, Y., Chen, Z., Chiclana, F., & Pedrycz, W. (2026). Enhancing multivariate time series forecasting for container reloading operations: An improved adaptive multi-granularity cascade forest model integrating. *Transportation Research Part E: Logistics and Transportation Review, 211*, Article 104847.

He, D., Wu, J., Jin, Z., Huang, C., Wei, Z., & Yi, C. (2025a). AGFCN: A bearing fault diagnosis method for high-speed train bogie under complex working conditions. *Reliab. Eng. Syst. Safe., 258*, Article 110907.

He, D., Zhao, J., Jin, Z., Huang, C., Zhang, F., & Wu, J. (2025b). Prediction of bearing remaining useful life based on a two-stage updated digital twin. *Advanced Engineering Informatics, 65*, Article 103123.

Hu, W., Dong, J., Yang, K., Ren, R., & Chen, Z. (2023). Network planning of metro-based underground logistics system against mixed uncertainties: A multi-objective cooperative co-evolutionary optimization approach. *Expert Systems with Applications, 217*, Article 119554.

Hu, W., Ren, R., Dong, J., Zhao, X., Hong, W., & Chen, Z. (2025). A state-of-the-art review of underground logistics systems: Research trends, application modes, planning approaches, and future directions. *Tunn. Undergr. Sp. Tech., 162*, Article 106641.

Transportation Technology Center Inc., 2010. General rules covering loading of carload shipmentsof commodities in closed cars.

Li, F., & Yuen, K. F. (2025). A systematic review on underground logistics system: Designs, impacts, and future directions. *Tunn. Undergr. Sp. Tech., 159*, Article 106483.

LIU, Y., DING, J., LI, Q., LI, F., LIU, J., 2025. A two-level model management-based surrogate-assisted evolutionary algorithm for medium-scale expensive multiobjective optimization. IEEE Transactions on Systems, Man, and Cybernetics: Systems.

Liu, Y., Liu, J., Ding, J., Yang, S., & Jin, Y. (2023). A surrogate-assisted differential evolution with knowledge transfer for expensive incremental optimization problems. *IEEE T. Evolut. Comput., 28*, 1039–1053.

Long, S., Zhang, Y., Deng, Q., Pei, T., Ouyang, J., & Xia, Z. (2022). An efficient task offloading approach based on multi-objective evolutionary algorithm in cloud-edge collaborative environment. *IEEE Transactions on Network Science and Engineering, 10*, 645–657.

Ministry of Housing and Urban Rural Development of the People's Republic of China, 2013. Code for design of metro.

Muñoz-Villamizar, A., Santos, J., Montoya-Torres, J. R., & Velázquez-Martínez, J. C. (2020). Measuring environmental performance of urban freight transport systems: A case study. *Sustainable cities and society, 52*, Article 101844.

Obrien, E. J., Zhang, L., Zhao, H., & Hajializadeh, D. (2018). Probabilistic bridge weigh-in-motion. *Can. J. Civil Eng., 45*, 667–675.

Peng, Y., Lu, S., Chen, F., Liu, X., & Tian, Z. (2024). Energy-efficient train control incorporating inherent reduced-power and hybrid braking characteristics of railway vehicles. *Transportation Research Part C: Emerging Technologies, 163*, Article 104626.

Rail WIM, 2020. http://https://www.is-wim.net/what-is-wim/wim-technologies/rail-wim/#content(accessed).

Scherbakov, A., Pushkarev, A., Kuzmin, O., Vinogradova, T., & Petrov, A. (2023). *Effects of bulk cargo displacements on changes in truck axle loads., 376*, 4027.

Scomet, E. (2023). Trees, forests, and impurity-based variable importance in regression. Annales de L'Institut Henri Poincare. *(B) Probabilites et statistiques, 1*, 21–52.

Singh, S. K., Das, A. K., Singh, S. R., & Racherla, V. (2023). Prediction of rail-wheel contact parameters for a metro coach using machine learning. *Expert Systems with Applications, 215*, Article 119343.

Sun, Z., He, D., He, Y., Shan, S., & Zhou, J. (2024). A bi-objective optimization model of metro trains considering energy conservation and passenger waiting time. *Journal of Cleaner Production, 437*, Article 140427.

Tan, Q., He, D., Sun, Z., Yao, Z., Zhou, J., & Chen, T. (2025). A deep reinforcement learning based metro train operation control optimization considering energy conservation and passenger comfort. *Engineering Research Express, 7*, 15252.

Tang, T., Luo, H., Song, Y., Fang, H., & Zhang, J. (2021). Chebyshev inclusion function based interval kinetostatic modeling and parameter sensitivity analysis for Exechon-like parallel kinematic machines with parameter uncertainties. *Mechanism and Machine Theory, 157*, Article 104209.

Tian, Y., Cheng, R., Zhang, X., Cheng, F., & Jin, Y. (2017). *An Indicator based Multi-Objective Evolutionary Algorithm with Reference Point Adaptation for Better Versatility*. PP: IEEE T. Evolut. Comput.

Visser, J.G., 2018. The development of underground freight transport: An overview. Tunn. Undergr. Sp. Tech. 80, 123-127.

Wu, J., He, D., Jin, Z., Zhao, M., Li, X., & Chen, Y. (2025). Multi-view fully connected graph to fuse multi-sensor signals for mechanical equipment remaining useful life prediction. *Journal of Manufacturing Systems, 80*, 1029–1052.

Wu, X., Li, G., Sun, Y., Wang, H., & Chen, Y. (2025). Theoretical and experimental exploration on the chattering control for the planar mechanism with clearance joint: Using an asymmetrically constrained vibro-impact absorber. *Mechanism and Machine Theory, 215*, Article 106171.

Xiao, Z., Murgovski, N., Chen, M., Feng, X., Wang, Q., & Sun, P. (2023). Eco-driving for metro trains: A computationally efficient approach using convex programming. *IEEE T. Veh. Technol., 72*, 10063–10076.

Xinhua News Agency. Unmanned vehicle + subway combined transport accelerates logistics before the holiday. http://news.fjsen.com/2025-01/27/content_31832175_0.htm(accessed).

Zhai, W., 2019. in: Vehicle–track coupled dynamics: theory and applications. Springer, p.

Zhai, W., Wang, K., & Cai, C. (2009). Fundamentals of vehicle-track coupled dynamics. *Vehicle Syst. Dyn., 47*, 1349–1376.

Zhang, Q., & Li, H. (2007). MOEA/D: A multiobjective evolutionary algorithm based on decomposition. *IEEE T. Evolut. Comput., 11*, 712–731.

Zhang, D., Clarke, D. B., Peng, Q., Gao, H., & Dong, C. (2019). *Effect of the combined centre of gravity on the running safety of freight wagons*. Dyn: Vehicle Syst.

Zhang, D., Tang, Y., Clarke, D. B., Peng, Q., & Dong, C. (2021a). An innovative method for calculating diagonal lashing force of cargo on railway wagons in a curve alignment. *Vehicle Syst. Dyn., 59*, 352–374.

Zhang, D., Tang, Y., Peng, Q., Dong, C., & Ye, Y. (2021b). Effect of mass distribution on curving performance for a loaded wagon. *Nonlinear Dynam., 104*, 2259–2273.

Zhang, D., Tang, Y., Sun, Z., & Peng, Q. (2022). Optimising the location of wagon gravity centre to improve the curving performance. *Vehicle Syst. Dyn., 60*, 1627–1641.

Zhang, D., Guo, Z., Ni, Y., Chen, Z., Ao, W. K., Bordbar, A., & Zhou, F. (2023a). Correlation between cargo properties and train overturning safety for a high-speed freight train under strong winds. *Eng. Appl. Comp. Fluid, 17*, Article 2221308.

Zhang, D., Tang, Y., & Peng, Q. (2023b). A novel approach for decreasing driving energy consumption during coasting and cruise for the railway vehicle. *Energy, 263*, Article 125615.

Zhang, D., Zhou, F., Tang, Y., Tao, Z., & Peng, Q. (2023c). Optimization of the loading plan for a railway wagon from the perspectives of running safety and energy conservation. *Energy, 280*, Article 128229.

Zhang, D., Tao, Z., Zhou, K., Zhou, F., Peng, Q., & Tang, Y. (2024a). Improving the energy efficiency and riding comfort of high-speed trains across slopes by the optimized suspension control. *Energy, 307*, 132660.

Zhang, D., Wang, S., Tang, Y., Ni, Y., Guo, J., & Peng, Q. (2024b). A novel method for evaluating load restraint assemblies to ensure the safety of railway freight transportation. *Sci. Rep.-UK, 14*, 4612.

Zhang, D., Zhou, F., Ao, W. K., Guo, Z., & Chen, Z. (2024c). Optimization of cargo distribution for high-speed freight trains to overcome strong wind conditions. *Eng. Appl. Comp. Fluid, 18*, 2434008.

Zhang, X., Gu, Y., Pei, W., & Jiang, Y. (2025). *AC transmission network expansion planning considering cascading failures and uncertainty of wind and photovoltaic energy*. Pow. Syst. Res.: Electr.

Zhang, Y., Li, S., He, C., Zhang, Y., Li, F., & Song, X. (2025). A surrogate-assisted multi-objective evolutionary algorithm with multiple reference points. *Expert Systems with Applications, 294*, Article 128670.

Zhang, P., Xu, L., Shi, T., Tang, Q., Song, L., Song, H., Yu, L., Deng, Z., Lou, P., & Yang, T. Y. (2026). Influences of seismic excitation and train speed on dynamic performance of train-track-bridge coupled system. *Journal of Railway Science and Technology.*

Zhou, F., Zhou, K., Zhang, D., & Peng, Q. (2024). Optimization of the cruising speed for high-speed trains to reduce energy consumed by motion resistances. *Appl. Energ., 374*, Article 124039.

Zitzler, E., Thiele, L., Laumanns, M., Fonseca, C. M., & da Fonseca, V. G. (2003). Performance assessment of multiobjective optimizers: An analysis and review. *IEEE T. Evolut. Comput., 7*, 117–132.

Zou, Y., Chu, X., Zhou, X., & Song, Z. (2025). Energy-efficient operation trajectory optimization of heavy-haul trains based on hybrid biological intelligent heuristic strategy. *Journal of Railway Science and Technology.*